Linking Intra-Plate Volcanism to Lithospheric Structure and Asthenospheric Flow

Thomas Duvernay[1], D. Rhodri Davies[1], Christopher Robert Mathews[1], Angus H. Gibson[1], and Stephan C Kramer[2]

[1]Australian National University
[2]Imperial College London

November 23, 2022

Abstract

Several of Earth's intra-plate volcanic provinces are hard to reconcile with the mantle plume hypothesis. Instead, they exhibit characteristics that are more compatible with shallower processes that involve the interplay between uppermost mantle flow and the base of Earth's heterogeneous lithosphere. The mechanisms most commonly invoked are edge-driven convection (EDC) and shear-driven upwelling (SDU), both of which act to focus upwelling flow and the associated decompression melting adjacent to steps in lithospheric thickness. In this study, we undertake a systematic numerical investigation, in both 2-D and 3-D, to quantify the sensitivity of EDC, SDU, and the associated melting to key controlling parameters. Our simulations demonstrate that the spatio-temporal characteristics of EDC are sensitive to the geometry and material properties of the lithospheric step, in addition to the magnitude and depth-dependence of upper mantle viscosity. These simulations also indicate that asthenospheric shear can either enhance or reduce upwelling velocities and the associated melting, depending upon the magnitude and orientation of flow relative to the lithospheric step. When combined, such sensitivities explain why step changes in lithospheric thickness, which are common along cratonic edges and passive margins, only produce volcanism at isolated points in space and time. Our predicted trends of melt production suggest that, in the absence of potential interactions with mantle plumes, EDC and SDU are viable mechanisms only for Earth's shorter-lived, lower-volume intra-plate volcanic provinces.

Linking Intra-Plate Volcanism to Lithospheric Structure and Asthenospheric Flow

Thomas Duvernay[1], D. Rhodri Davies[1], Christopher R. Mathews[1], Angus H. Gibson[1], Stephan C. Kramer[2]

[1]Research School of Earth Sciences, The Australian National University, Canberra, ACT, Australia
[2]Department of Earth Science and Engineering, Imperial College London, London, UK

Key Points:

- Edge-driven convection is sensitive to upper-mantle viscosity and the geometry and material properties of lithospheric steps.
- Asthenospheric flow magnitude and orientation dictate whether edge-driven cells are enhanced through asthenospheric shear or suppressed.
- Melting associated with edge-related processes can account for Earth's shorter-lived and lower-volume intra-plate volcanic provinces.

Corresponding author: Thomas Duvernay, `thomas.duvernay@anu.edu.au`

Abstract

Several of Earth's intra-plate volcanic provinces are hard to reconcile with the mantle plume hypothesis. Instead, they exhibit characteristics that are more compatible with shallower processes that involve the interplay between uppermost mantle flow and the base of Earth's heterogeneous lithosphere. The mechanisms most commonly invoked are edge-driven convection (EDC) and shear-driven upwelling (SDU), both of which act to focus upwelling flow and the associated decompression melting adjacent to steps in lithospheric thickness. In this study, we undertake a systematic numerical investigation, in both 2-D and 3-D, to quantify the sensitivity of EDC, SDU, and the associated melting to key controlling parameters. Our simulations demonstrate that the spatio-temporal characteristics of EDC are sensitive to the geometry and material properties of the lithospheric step, in addition to the magnitude and depth-dependence of upper mantle viscosity. These simulations also indicate that asthenospheric shear can either enhance or reduce upwelling velocities and the associated melting, depending upon the magnitude and orientation of flow relative to the lithospheric step. When combined, such sensitivities explain why step changes in lithospheric thickness, which are common along cratonic edges and passive margins, only produce volcanism at isolated points in space and time. Our predicted trends of melt production suggest that, in the absence of potential interactions with mantle plumes, EDC and SDU are viable mechanisms only for Earth's shorter-lived, lower-volume intra-plate volcanic provinces.

Plain Language Summary

Intra-plate volcanoes, which occur away from plate boundaries, are common across Earth's surface (e.g. Hawaii, Reunion, Cameroon, Eastern Australia), but their origin remains debated. The classically invoked hypothesis for their genesis centres around mantle plumes – buoyant columns of hot rock that ascend through Earth's mantle. Upon reaching the base of tectonic plates, plumes generate extensive melting and remain comparatively fixed, providing a mechanism for generating linear volcanic tracks that grow older in the direction of plate motion. Several intra-plate volcanic regions, however, exhibit characteristics that are inconsistent with the mantle plume hypothesis: their eruptions are usually short-lived, non-age-progressive, and only generate minor volumes of lava. Therefore, they are more likely to be driven by shallower processes, such as small-scale convective instabilities that develop adjacent to step-changes in the thickness of Earth's lithosphere, its rigid outermost shell. In this study, we utilise both 2-D and 3-D computational models to simulate these shallow processes, and we analyse their sensitivity to a range of key controlling parameters. Our results help to solve the puzzle of why such processes only produce volcanism at isolated locations and, in the absence of interactions with mantle plumes, limit their applicability to Earth's shorter-lived, lower-volume volcanic provinces.

1 Introduction

Most of Earth's volcanism is concentrated at tectonic plate boundaries, representing the surface manifestation of either passive decompression melting at mid-ocean ridges (e.g. Sengör & Burke, 1978; Phipps Morgan et al., 1987) or volatile-induced melting at subduction zones (e.g. Tatsumi et al., 1986; Peacock, 1990). However, a significant and widespread class of volcanism occurs within plates or across plate boundaries. These so-called *intra-plate* volcanic provinces cannot be explained through plate tectonic processes and require an alternative generation mechanism. Mantle plumes – hot, buoyant columns that rise from Earth's core-mantle boundary to its surface (e.g. Morgan, 1971) – are commonly invoked to explain age-progressive volcanic tracks that grow older in the direction of plate motion. At the young end of these tracks, volcanism localises within a radius of a few tens of kilometres and has persisted for tens of millions of years, implying a self-renewing source that lies below the region where the mantle moves with the surface plate (e.g. Richards et al., 1989; Farnetani & Richards, 1995; Courtillot et al., 2003; Davies & Davies, 2009; French & Romanowicz, 2015). Classic examples include the volcanic tracks terminating at Hawaii in the Pacific, Reunion in the Indian Ocean and Cosgrove in eastern Australia (e.g. Duncan & Richards, 1991; Davies et al., 2015; Jones et al., 2017; Bredow et al., 2017). However, many intra-plate volcanic provinces are hard to reconcile with the mantle plume hypothesis, for example the Colorado Plateau in North America, the Moroccan Atlas Mountains in northern Africa and the Newer Volcanics Province of southeastern Australia (e.g. Demidjuk et al., 2007; Missenard & Cadoux, 2012; Davies & Rawlinson, 2014; Klöcking et al., 2018). At these locations, volcanism is often short-lived (< 20 Myr), non-age-progressive, and of low eruptive volume, all of which point towards alternative generation mechanisms (e.g. King & Ritsema, 2000; Conrad et al., 2011; Davies & Rawlinson, 2014; Ballmer et al., 2015).

Most proposed mechanisms involve the interplay between shallow mantle flow and the base of Earth's heterogeneous lithosphere. The two most commonly invoked are (i) edge-driven convection (EDC) – a small-scale convective instability, associated with a step in lithospheric thickness, driven by lateral density variations between a thick lithosphere and adjacent asthenosphere (e.g. Buck, 1986; King & Anderson, 1998; King & Ritsema, 2000; Till et al., 2010; Davies & Rawlinson, 2014; Ballmer et al., 2015; Liu & Chen, 2019); and (ii) shear-driven upwelling (SDU) – defined here as a sub-lithospheric ascending flow, induced by topography at the base of the lithosphere in the presence of asthenospheric shear (e.g. Conrad et al., 2010, 2011; Bianco et al., 2011; Davies & Rawlinson, 2014; Ballmer et al., 2015). For the latter, we acknowledge that Conrad et al. (2010) formulated SDU in the context of low-viscosity pockets within the shallow asthenosphere, but we focus solely on the role of lithospheric topography herein. While both EDC and SDU have been linked to the generation of intra-plate volcanism, their applicability and relative importance remain unclear and likely vary from one volcanic province to the next, owing to regional differences in their primary controlling parameters (e.g. King & Ritsema, 2000; Conrad et al., 2011; Davies & Rawlinson, 2014). To complicate matters further, EDC and SDU may interact with upwelling mantle plumes and pockets of low-viscosity asthenosphere to produce intricate volcanic patterns at the surface (e.g. Conrad et al., 2011; Davies et al., 2015; Kennett & Davies, 2020).

To better assess the origin of some of Earth's intra-plate volcanic provinces and understand possible interactions between different driving mechanisms, it is necessary to analyse, in isolation, how EDC, SDU, and their associated melting depend on several plausible controlling parameters. Accordingly, in this study, we use a systematic series of 2-D and 3-D numerical models to quantify the sensitivity of EDC and SDU to a subset of these parameters. We focus on the role of (i) the topography of the lithosphere-asthenosphere boundary (LAB), especially the geometry and orientation of lithospheric steps and their material properties; (ii) uppermost mantle viscosity, both in terms of its magnitude and depth-dependence; and (iii) the intensity, depth distribution and orientation of plate motion and asthenospheric flow. These models allow us to identify the fundamental controls on shallow edge-related processes and highlight, in particular, what determines the location and intensity of melt production at depth. Our results allow us to place quantitative bounds on the conditions under which EDC and SDU can explain intra-plate volcanism in the absence of other melt-generating processes.

2 Methods

2.1 Governing Equations and Solution Strategy

We set up a numerical study of thermo-chemical convection applied to Earth's mantle in both 2-D and 3-D Cartesian domains with dimensions 4000:[4000]:1000 km (x:[y]:z). We use Fluidity – a finite-element, control-volume computational modelling framework (e.g. Davies et al., 2011; Kramer et al., 2012) – to solve the equations governing mantle convection for pressure, velocity, temperature and material volume fraction fields, on anisotropic, adaptive, simplex meshes. Mesh optimisation is controlled by a metric that depends on the Hessian of the temperature, velocity and material volume fraction fields. It provides increased resolution in areas of dynamical significance, with coarser resolution elsewhere, thus ensuring computational efficiency whilst maintaining solution accuracy (e.g. Davies et al., 2007). The resulting mesh satisfies a minimum edge-length condition of 5 km, a maximum edge-length of 200 km and a 20 % edge-length gradation (i.e. the maximum allowable jump in edge-length from element to element).

We simulate incompressible (Boussinesq) Stokes flow in an Eulerian reference frame, incorporating spatial variations of viscosity. In this context, we solve the following governing equations:

$$0 = \nabla \cdot \boldsymbol{u}, \tag{1}$$

$$\boldsymbol{0} = \nabla p - \nabla \cdot \left[\mu\Big(\nabla\boldsymbol{u} + (\nabla\boldsymbol{u})^{\mathsf{T}}\Big)\right] + \Big[\rho_0\alpha\big(T - T_S\big) - \Delta\rho_c\Big]\boldsymbol{g}, \tag{2}$$

$$\mu = \left[A_1 \times \exp\left(-\frac{E^* + \rho_0 g z\, V_1^*}{RT^*}\right) + A_2 \times \exp\left(-\frac{E^* + \rho_0 g z\, V_2^*}{RT^*}\right)\right]^{-1}, \tag{3}$$

$$T^* = T + \psi z. \tag{4}$$

We model energy conservation through a simple advection-diffusion equation including a heat source term:

$$\frac{\partial T}{\partial t} + \boldsymbol{u} \cdot \nabla T = \kappa \Delta T + \phi. \tag{5}$$

Distinct materials are initialised and tracked using material volume fraction fields (Wilson, 2009; Garel et al., 2014), described by a linear advection equation:

$$\frac{\partial \Gamma}{\partial t} + \boldsymbol{u} \cdot \nabla \Gamma = 0. \tag{6}$$

In the above equations, $\boldsymbol{u}$ denotes velocity, p dynamic pressure, μ dynamic viscosity, T temperature, z depth, ρ density, $\Delta\rho_c$ the density contrast between different materials, and Γ volume fraction. Other symbol names and values are presented in Tables 1 and 2. Although our models are incompressible, when determining viscosity, we update temperature to account for an adiabatic gradient (Equation 4); a similar update is performed to determine melt fractions (Section 2.4). Our computational domain includes three different materials: continental crust, continental lithosphere (excluding the crust) and mantle (incorporating oceanic lithosphere). Each has a distinct density (Table 1; Artemieva, 2009), but they all obey the same viscosity law, albeit with continental lithosphere that is intrinsically 100 times more viscous than adjacent mantle (e.g. Lenardic & Moresi, 1999; Currie & van Wijk, 2016).

2.2 2-D Reference Case

We begin by simulating idealised 2-D flow around thermally and compositionally-defined steps in lithospheric thickness, which separate thick continental lithosphere from thin oceanic lithosphere – this is analogous to a passive margin setting.

We consider viscosity, μ, to be isotropic and model it through a diffusion creep rheology. To describe this mechanical behaviour, we combine two empirical Arrhenius laws (Hirth & Kohlstedt, 2004; Korenaga & Karato, 2008) inside which we account for both the temperature increase through the adiabatic gradient, ψ, and the effect of lithostatic pressure (Equations 3 and 4). We fix a common activation energy, $E^* = 350\,\mathrm{kJ\,mol^{-1}}$, for both laws but vary the activation volumes, V_i^*, and viscosity pre-factors, A_i. Setting distinct V_1^* and V_2^* in Equation 3 allows us to incorporate a low-viscosity channel in the

Table 1. *Model parameters common to all simulations*

Name	Symbol	Value	Units
Reference Density	$\rho_0 \,\vert\, \rho_0^{Cont} \,\vert\, \rho_0^{Crust}$	3370 | 3300 | 2900[a]	$\mathrm{kg\,m^{-3}}$
Gravity	g	9.8	$\mathrm{m\,s^{-2}}$
Gas Constant	R	8.3145	$\mathrm{J\,K^{-1}\,mol^{-1}}$
Thermal Expansion	α	3×10^{-5}[b]	$\mathrm{K^{-1}}$
Surface Temperature	T_S	290	K
Mantle Temperature	T_M	1650[c,d]	K
Adiabatic Gradient	ψ	4×10^{-4}[e]	$\mathrm{K\,m^{-1}}$
Thermal Diffusion	κ	6×10^{-7}[f]	$\mathrm{m^2\,s^{-1}}$
Internal Heating (Cont. Crust)	ϕ	2.6×10^{-13}[g]	$\mathrm{K\,s^{-1}}$
Internal Heating (Elsewhere)	ϕ	4×10^{-15}[h]	$\mathrm{K\,s^{-1}}$
Activation Energy	E^*	350[i]	$\mathrm{kJ\,mol^{-1}}$
Upper Mantle Viscosity at ULMB	μ_{660}	10^{21}	Pa s
Lower Mantle Viscosity	μ_{LM}	2×10^{22}	Pa s
Viscosity Bounds	$\mu_{min} \,\vert\, \mu_{max}$	$10^{18} \,\vert\, 10^{24}$	Pa s
Water Content (Melting)	X_{H_2O}	300	ppm

Note. Parameters for the rheological law are guided by Korenaga and Karato (2008); additional values used in the upper mantle can be found in Table 2.
[a] Artemieva (2009). [b] Ye et al. (2009). [c] Putirka (2016). [d] Sarafian et al. (2017). [e] Katsura et al. (2010). [f] Gibert et al. (2003). [g] $\equiv 1.3 \times 10^{-6}\,\mathrm{W\,m^{-3}}$ (Jaupart & Mareschal, 2005). [h] $\equiv 2 \times 10^{-8}\,\mathrm{W\,m^{-3}}$ (Pollack & Chapman, 1977). [i] A value of $550\,\mathrm{kJ\,mol^{-1}}$ is used for the dislocation creep regime (Section 2.3.1).

sub-lithospheric mantle (e.g. Richards et al., 2001). Conversely, specifying identical parameters leads to a single law with a pre-factor twice as large. Either way, to determine V_i^* and A_i and, thereby, establish our upper mantle viscosity profile, we consider the thermal structure generated by a half-space cooling model (Parsons & Sclater, 1977) of age 40 Myr. Then, we define target values that the profile should satisfy: (i) μ_{660}, the value at the upper-lower mantle boundary (ULMB), which we set to 10^{21} Pa s (e.g. Mitrovica & Forte, 2004); and (ii) μ_{min}^0, the profile's minimum value in the sub-lithospheric mantle (e.g. Iaffaldano & Lambeck, 2014). Using these constraints, we iteratively determine the values of A_i and V_i^* (Table 2). To complete our profile, we fix the lower-mantle viscosity, μ_{LM}, to 2×10^{22} Pa s, resulting in a factor of 20 increase through the ULMB. Finally, we restrict viscosity values between $\mu_{min} = 10^{18}$ Pa s and $\mu_{max} = 10^{24}$ Pa s. The resulting reference profile (representative of our initial oceanic domain), alongside the other profiles examined (Section 2.3.1), are illustrated in Figure 1a. All profiles are compatible with estimates derived from models of global isostatic adjustment (e.g. Paulson & Richards, 2009).

For our reference model, we impose no-slip velocity boundary conditions at the bottom of the domain and free-slip boundary conditions elsewhere. Temperature is set to $T_S = 290\,\mathrm{K}$ at the surface and $T_M = 1650\,\mathrm{K}$ at the base, with insulating sidewalls – $\frac{\partial T}{\partial n} = 0$. Initial temperature conditions incorporate a sub-lithospheric mantle of temperature T_M and differentiate between oceanic and continental realms (Figure 1c). Oceanic lithosphere is treated as a surface thermal boundary layer, where the temperature distribution follows a half-space cooling model of age 40 Myr; the 1620 K isotherm, which we use to identify the LAB, is located at a depth of 90 km. Thicker continental lithosphere, including a 41 km-thick crust, extends down to 200 km depth and is described by a conductive geotherm (e.g. Pollack & Chapman, 1977), which we determine by solving a 1-D steady-state heat equation. We use a value of $3\,\mathrm{W\,m^{-1}\,K^{-1}}$ for the thermal conductivity (Schatz & Simmons, 1972) and account for internal heat generation through an exponential decrease of characteristic length-scale 9 km (e.g. Lachenbruch, 1970). We set the surface crustal heat production to $6 \times 10^{-6}\,\mathrm{W\,m^{-3}}$ (McLaren et al., 2003), which is compatible with the internal heating, ϕ, defined in Equation 5 as it yields a comparable heat flux upon spatial integration (Nicolaysen et al., 1981; Jaupart & Mareschal, 2005). Oceanic and continental segments are connected via two 200 km-wide thermo-chemical steps located between 1150 km and 1350 km to the left, and 2650 km and 2850 km to the right of the continent; the material boundary is halfway through both steps. Within these steps, the depth of a given isotherm follows an error function of the horizontal coordinate, x. Such a definition ensures a smooth, diffusive transition between the continental area and adjacent lithosphere (Figure 1c), and it leads to instabilities that develop as they would naturally do in this type of system.

2.3 Parameter Space

2.3.1 2-D Cases

To assess possible expressions of flow adjacent to lithospheric steps, we first conduct a systematic study around our reference case, exploring the effect of varying val-

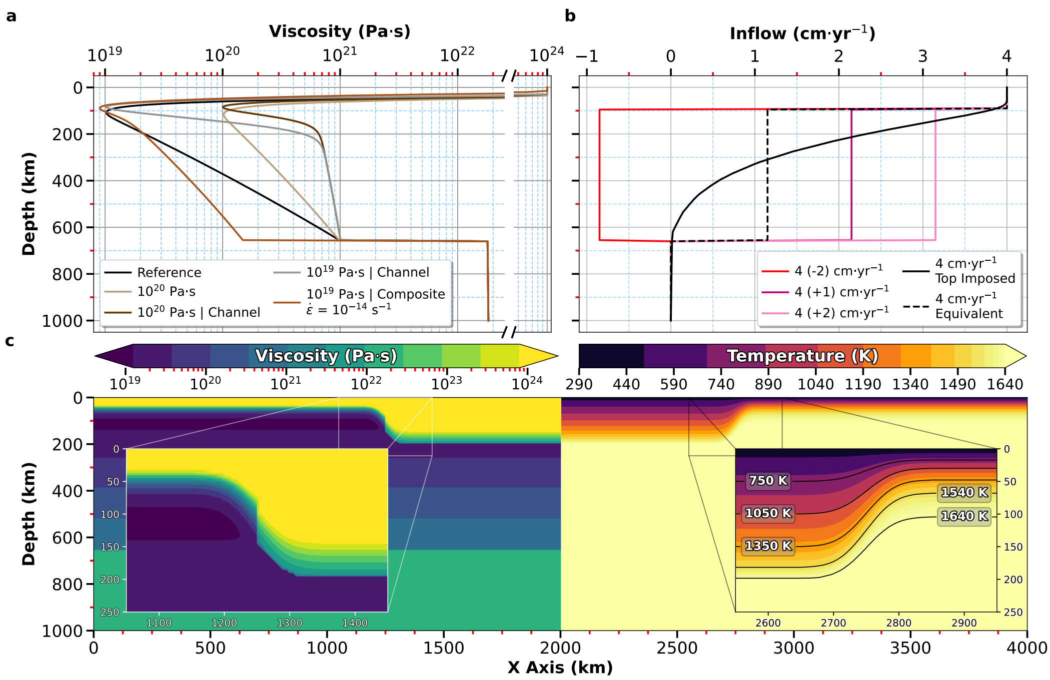

Figure 1. 2-D model setup: (a) Viscosity profiles considered in the 2-D parameter space study, calculated according to the temperature distribution of the reference 40 Myr old oceanic lithosphere. These profiles are for representation purposes only: our models include strong lateral viscosity contrasts. (b) Velocity profile within the oceanic realm resulting from a purely plate-driven model (solid black line) and its simplified counterpart (dashed black line), which is used as a basis for inflow boundary conditions (Section 2.3.1). Remaining profiles incorporate additional asthenospheric shear (number between parentheses), either aligned with (+ sign) or opposite to (- sign) the direction of plate motion. (c) Initial distribution of viscosity (left) and temperature (right) inside the 2-D domain. The viscosity inset illustrates the separation between continent and ocean through the $\times 100$ continental viscosity increase, while the temperature inset highlights the smooth paths taken by isotherms at the step.

Table 2. *Model Parameters Varied Across 2-D Simulations*

Geometry

Name (Abbreviation)	Values	Units
Oceanic Lithosphere Age (Oce.)	20 and **40**	Myr
Continent Depth (Cont.)	140 and **200**	km
Step Width (Step)	**200** and 400	km
Step Material Proportion (Step)	**Equal** and $\frac{2}{3}$ Oce.	–

Viscosity[a]

Profile[b]	Minimum viscosity μ^0_{min} (Pa s)	Channel	Activation volume V_1^*, V_2^* ($m^3\,mol^{-1}$)[c]	Pre-factor A_1, A_2 (Pa s)[c]
	$\mathbf{10^{19}}$	**No**	$\mathbf{6.8 \times 10^{-6}}$	$\mathbf{1.9 \times 10^{-8}}$
	10^{19}	Yes	25×10^{-6}, 3×10^{-6}	2.1×10^{-6}, 2.1×10^{-10}
	10^{20}	No	4.7×10^{-6}	1.1×10^{-9}
	10^{20}	Yes	25×10^{-6}, 3×10^{-6}	2×10^{-7}, 2.1×10^{-10}

Plate Motion

Name	Values	Units
Plate Speed	**0**, 2, 4 and 6	$cm\,yr^{-1}$
Additional Shear	−2, **0**, 1 and 2	$cm\,yr^{-1}$

Note. Reference case values are in bold.
[a] Diffusion creep regime only; refer to Section 2.3.1 for the composite regime.
[b] Refer to Figure 1a for visualisation of the profiles.
[c] In the absence of a channel, activation volumes and pre-factors are identical in both laws (Equation 3).

ues for potential key controlling parameters (Table 2). We vary four geometric parameters: the initial age of oceanic lithosphere (i.e. the thickness of the lithospheric lid), the depth of the continent (i.e. the extent of the continental guide), the width of the lithospheric step (effectively changing its slope), and the location of the material interface between continent and ocean within the step (modifying the density distribution within the step). We also examine cases with five distinct viscosity configurations (Figure 1a): four account for diffusion creep only, as described in Section 2.2, and differ in their value of μ^0_{min} and the inclusion or exclusion of a sub-lithospheric viscosity channel (Table 2), while the remaining case accounts for deformation through a composite diffusion and dislocation creep rheology, calculated via a harmonic mean:

$$\mu = 2 \times \left(\frac{1}{\mu_{diff}} + \frac{1}{\mu_{disl}} \right)^{-1}. \tag{7}$$

The diffusion creep component, μ_{diff}, is identical to the reference case (Equation 3), while the dislocation creep component, μ_{disl}, introduces a (non-linear) dependence on the second invariant of the strain-rate tensor, $\dot{\epsilon}_{II}$, according to

$$\mu_{disl} = \left[A \times \dot{\epsilon}_{II}^{\frac{n-1}{n}} \times \exp\left(-\frac{E^* + \rho_0 g z V^*}{nRT^*} \right) \right]^{-1}. \tag{8}$$

For dislocation creep, we increase the activation energy to $550\,kJ\,mol^{-1}$, the activation volume to $12 \times 10^{-6}\,m^3\,mol^{-1}$ and set the values of A and n to 2.2×10^{-4} Pa s and 3.6 respectively, guided by Korenaga and Karato (2008).

In addition, we investigate the effect of plate motion and asthenospheric shear through kinematic boundary conditions. We first consider purely plate-driven cases by imposing horizontal motion of 2, 4 and 6 cm yr^{-1} at the surface and opening both side boundaries (whilst imposing a lithostatic pressure condition); the flow generated is akin to a classical Couette profile. We subsequently explore the effect of asthenospheric shear whilst keeping plate motion imposed. To do so, we consider the horizontal velocity profile generated within the oceanic realm in the 4 cm yr^{-1} plate-driven case (solid black line, Figure 1b) and generate an equivalent, albeit simplified, profile. We impose a constant velocity, equal to the plate speed, from the surface down to the LAB at 90 km depth, and we close side-boundaries in the lower mantle. For the upper mantle, we integrate the plate-driven velocity profile between depths of 90 km and 660 km, and average the result over that depth range. Using the obtained value (≈ 1.15 cm yr^{-1}) as an asthenospheric inflow boundary condition (dashed black line, Figure 1b), we replicate the dynamical behaviour produced by the plate-driven case (Figures S1 and S2), demonstrating that results are largely insensitive to the depth-dependence of the inflow profile prescribed within the asthenosphere – the flow is redistributed in line with the underlying physics. Subsequently, to provide additional shear either in the direction of plate motion, or opposite to it, we increase, or decrease, the constant asthenospheric flow by 2 cm yr^{-1}. Additionally, to illustrate the balance between the plate-driven flow and asthenospheric shear, we include a case with a smaller 1 cm yr^{-1} increase (Figure 1b). For completeness, we also consider an end-member case that incorporates shear only by using our increased asthenospheric flow scenario and setting the coefficient of thermal expansion to zero, which prevents the development of edge-driven instabilities. For all cases incorporating plate motion, we prescribe the temperature at the inflow boundary using the initial thermal structure of oceanic lithosphere. We also increase the domain size from 4000 km to 6000 km to prevent any interaction between the continental block and sidewalls of the domain.

2.3.2 3-D Cases

We extend our analyses to 3-D to quantify the sensitivity of EDC and SDU to more complex continental geometries and a broader spectrum of plate motion and asthenospheric flow directions, relative to the continent. Other model parameters remain identical to our reference 2-D case.

We examine four continental geometries for which the shape of the continent is based on a 200 km-thick cuboid located between x, y = 1250 km and x, y = 2750 km (Figure 2). Similar to our 2-D models, lithospheric steps connect continent to ocean along continental boundaries, including the four 'corners'. Each case differs in the following way: (i) *Case U400* incorporates a 400 km-wide oceanic indent inside the continent, between x = 2350 km, y = 1800 km and x = 2750 km, y = 2200 km, with additional steps at inner edges and corners; (ii) *Case U600* is similar to Case U400, albeit with a wider indent of 600 km, located between x = 2150 km, y = 1700 km and x = 2750 km, y = 2300 km; (iii) *Case U400-Grad* builds on Case U400 but differs by the presence of a linear gradient in the y-direction, from z = 130 km to z = 230 km depth, to represent the continental LAB; (iv) *Case Complex* does not incorporate an indent but, instead, combines a similar gradient as Case U400-Grad (same direction, different amplitude) with sinusoidal variations and local anomalies to define the continental LAB. In particular, the smaller-scale variations in LAB topography included in Case Complex allow us to investigate the flow regime and melt patterns in a more realistic scenario that better approximates the nature of the LAB inferred through seismic techniques and probabilistic inversion of combined geophysical datasets (e.g. Afonso et al., 2016; Rawlinson et al., 2017).

To explore the effects of background asthenospheric flow, we select Case U400 as our basis and impose both plate motion and asthenospheric inflow in four different directions: positive x at x = 0 km, negative x at x = 6000 km, positive y at y = 0 km and both positive x and y (which we will refer to as oblique) at x, y = 0 km. We follow the same strategy to produce the velocity inflow profile as for our 2-D cases but only consider 4 cm yr^{-1} plate motion with a 2 cm yr^{-1} increase of the constant asthenospheric in-

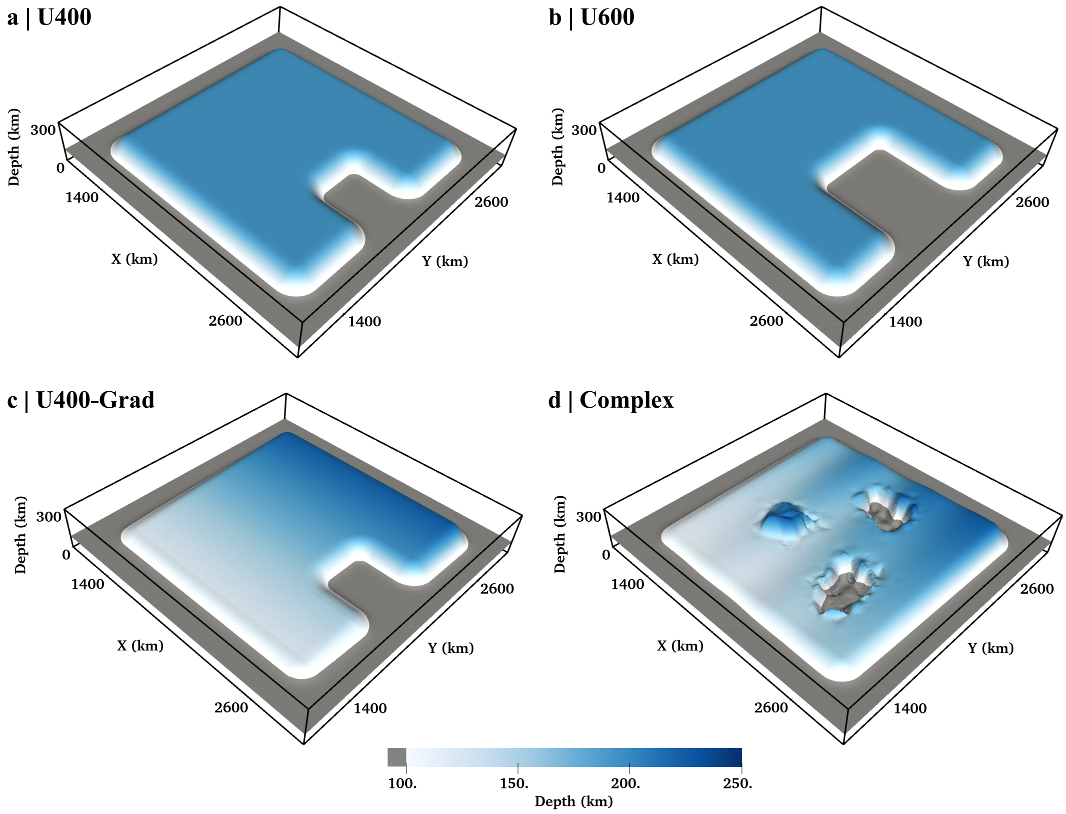

Figure 2. Initial topography of the LAB, as delineated by the 1620 K isotherm, for continental geometries used in our 3-D simulations. On each panel, the view is from below, looking at the base of the continent. (a) Case U400. (b) Case U600. (c) Case U400-Grad. (d) Case Complex.

flow (Section 2.3.1). In the oblique case, we also apply the inflow profile at the outflow boundaries to ensure flow remains oblique inside the domain.

2.4 Model Diagnostics

2.4.1 Edge-Driven Cells

For our 2-D cases, we identify the edge-driven cells generated adjacent to steps in lithospheric thickness and quantify their strength. When plate motion and asthenospheric shear are imposed, we uncover cells by subtracting from the velocity field a vertical profile of u_x, sampled through the centre of the continental realm. Following Coltice et al. (2018), we calculate at each mesh node the angle of the velocity vector relative to the x-axis and the horizontal derivative of the vertical component of velocity, $\frac{\partial u_z}{\partial x}$. We next divide the domain into large squares inside which we analyse angle and derivative values. For a cell to exist, velocity vectors must be oriented such that they form the shape of an ellipse. Accordingly, we require the equivalent condition that vector directions distribute in all four quadrants of the unit circle, which we interpret in terms of the distribution of angles. Moreover, we apply a threshold to the absolute value of the derivative (e.g. $3 \times 10^{-15}\,\mathrm{s}^{-1}$ for the reference viscosity profile), filtering out squares with only low-intensity features. We test each square for both conditions and either discard those that do not meet our criteria or decompose others into four sub-squares. We iterate through the process until we reach the desired threshold of squares with 10 km sides. At this stage, we consider the remaining squares to contain the centre of a cell, approximately defined by the square's centroid. With the centre of each cell accurately known, relevant velocity profiles can be drawn and compared across multiple cases.

2.4.2 Melting

To track the occurrence of melting, we use the particle-in-cell method recently implemented and validated in Fluidity (Mathews, 2021). We adopt the batch melting parameterization for wet upper-mantle peridotite from Katz et al. (2003), which addresses both the exhaustion of clinopyroxene and water saturation in the rock. Our implementation considers the pressure to be lithostatic, incorporates the adiabatic temperature increase with depth (similar to our viscosity formulation) and makes use of an algorithm for root-finding (Brent, 2013). Moreover, to account for the latent heat of fusion, we couple the melting parameterisation of Katz et al. (2003) to a modified version of the thermodynamic framework from McKenzie (1984) (Supplementary Information).

Particles are randomly initialised throughout the domain, with a denser distribution adjacent to lithospheric steps where melting is expected. We typically use 2×10^5 and 2×10^7 particles in 2-D and 3-D simulations, respectively. For each particle, we determine the onset of melting and track the evolution of both melt fraction, F, and the temperature change due to the latent heat of fusion. At the beginning of the simulation, F is calculated according to the pressure and temperature conditions of the initial state. Particles subsequently record a new value of F at each time-step and keep track of the maximum value experienced, F_{max}, with melting only occurring when the current F is greater than any previous F (i.e. $F > F_{max}$). A melting rate, M, is calculated using the current time-step, δt:

$$M = max\left(0, \frac{F - F_{max}}{\delta t}\right). \tag{9}$$

As melting occurs, the temperature on a particle not only varies according to the local temperature gradient but also changes through latent heating; both contributions can be distinguished. Consequently, temperatures on nodes of the underlying finite element mesh are updated through the source term of the heat equation (Equation 5). We do not attempt to simulate melt extraction or 're-freezing'.

For all simulations, we calculate the cumulative melt production beneath a region of interest, surrounding the continent. To do so, at each time-step, we select particles within a given depth range where melting is occurring (e.g. between 30 km and 160 km) and construct a piecewise linear interpolant from the obtained melting rate. We then evaluate the interpolant onto a 5 km-resolution structured grid and use Simpson's rule to integrate along any space dimension, as well as multiply by the current model time-step to integrate in time. We obtain cumulative melt thicknesses/areas/volumes by summing results from each time-step. To account for continental motion in cases with a prescribed inflow, we advect the grid according to the displacement of a particle that is located within the rigid continent. We ignore melting from the first time-step as it represents an equilibration process between the originally unmolten rocks and the pressure-temperature-velocity conditions of the model.

3 Results

3.1 Two-Dimensional Simulations

We first examine results from our 2-D simulations. Our reference case incorporates 40 Myr old oceanic lithosphere, a 200 km thick continent and 200 km wide steps, with the material interface between continent and ocean halfway along the step. The initial viscosity distribution, purely in the diffusion creep regime, reaches a minimum of 10^{19} Pa s in the sub-lithospheric oceanic mantle and does not include a low-viscosity channel; domain boundaries are closed.

We focus on the dynamics at the right step, illustrated for 30 Myr in Figure 3. A cell-like flow develops, adjacent to the continent, driven by the negative buoyancy of oceanic material at the step. Flow rapidly intensifies, with peak vertical velocities increasing by a factor of ∼3 from 7 to 15 Myr. Continental lithosphere, owing to its lower density and increased viscosity, guides downward motion that, in turn, generates upwelling beneath adjacent oceanic lithosphere. A secondary instability initiates away from the step after ∼15 Myr and persists throughout the remainder of the model's evolution. Melting occurs where upwelling material impinges beneath oceanic lithosphere, leading to melting rates of, on average, a few 100 ppm Myr^{-1}, with some particles recording over ∼1 ‰ Myr^{-1} at 30 Myr; melt fractions reach maximum values of 1 %. Melting is initially induced by the main edge-driven flow and subsequently sustained by the secondary instability, which delays lithospheric thickening and locally enhances upwelling velocities.

We next examine the role of background asthenospheric flow using a 4 cm yr^{-1} plate-driven case, alongside two cases with additional 2 cm yr^{-1} shear in the asthenosphere, aligned with, or opposite to, the direction of plate motion, and a similar case with 2 cm yr^{-1} shear aligned with plate motion for which the coefficient of thermal expansion is set to 0. Figure 4 compares the dynamics around both lithospheric steps after 20 Myr, with arrow glyphs illustrating a modified velocity field: the horizontal component is relative to

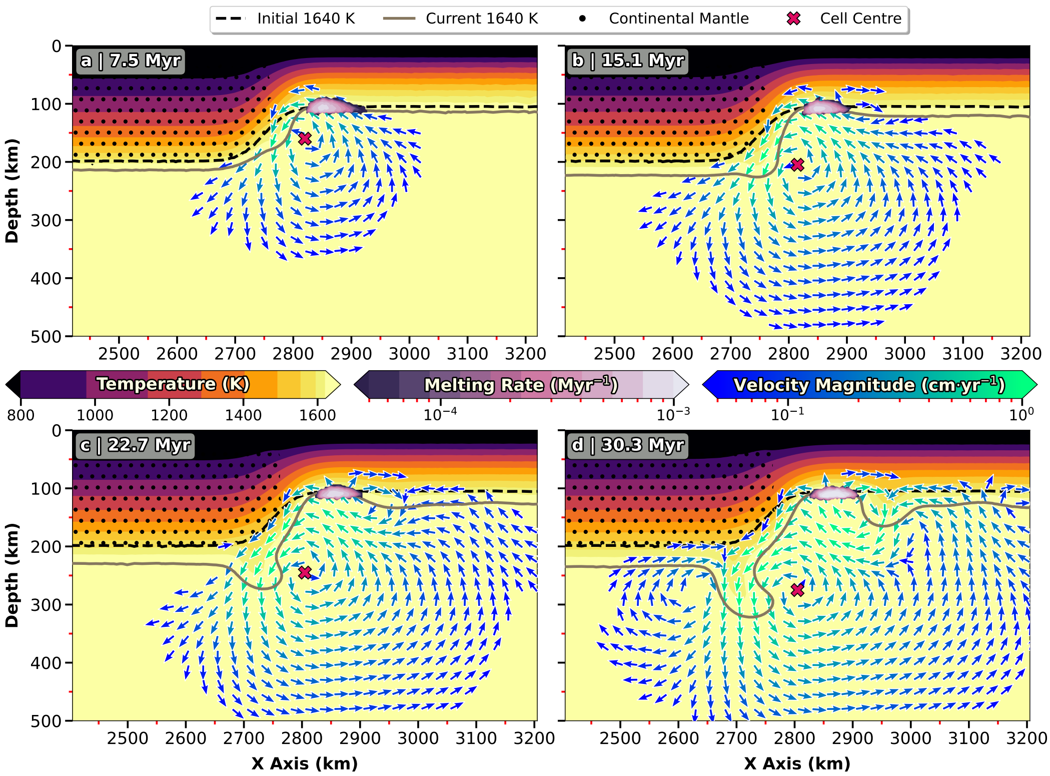

Figure 3. Development of an instability adjacent to the right step of the reference 2-D case. Background colours represent temperature, with the current and initial location of the 1640 K isotherm – a convenient proxy for downwellings – highlighted by solid grey and dashed black lines, respectively. Black dots depict the location of continental mantle. Arrow glyphs highlight the areas of most intense velocity, where the magnitude is higher than 0.5 mm yr^{-1}, as indicated by their colour. Areas experiencing melting are represented as a superimposed surface, coloured by melting rate. The red cross denotes the centre of the cell.

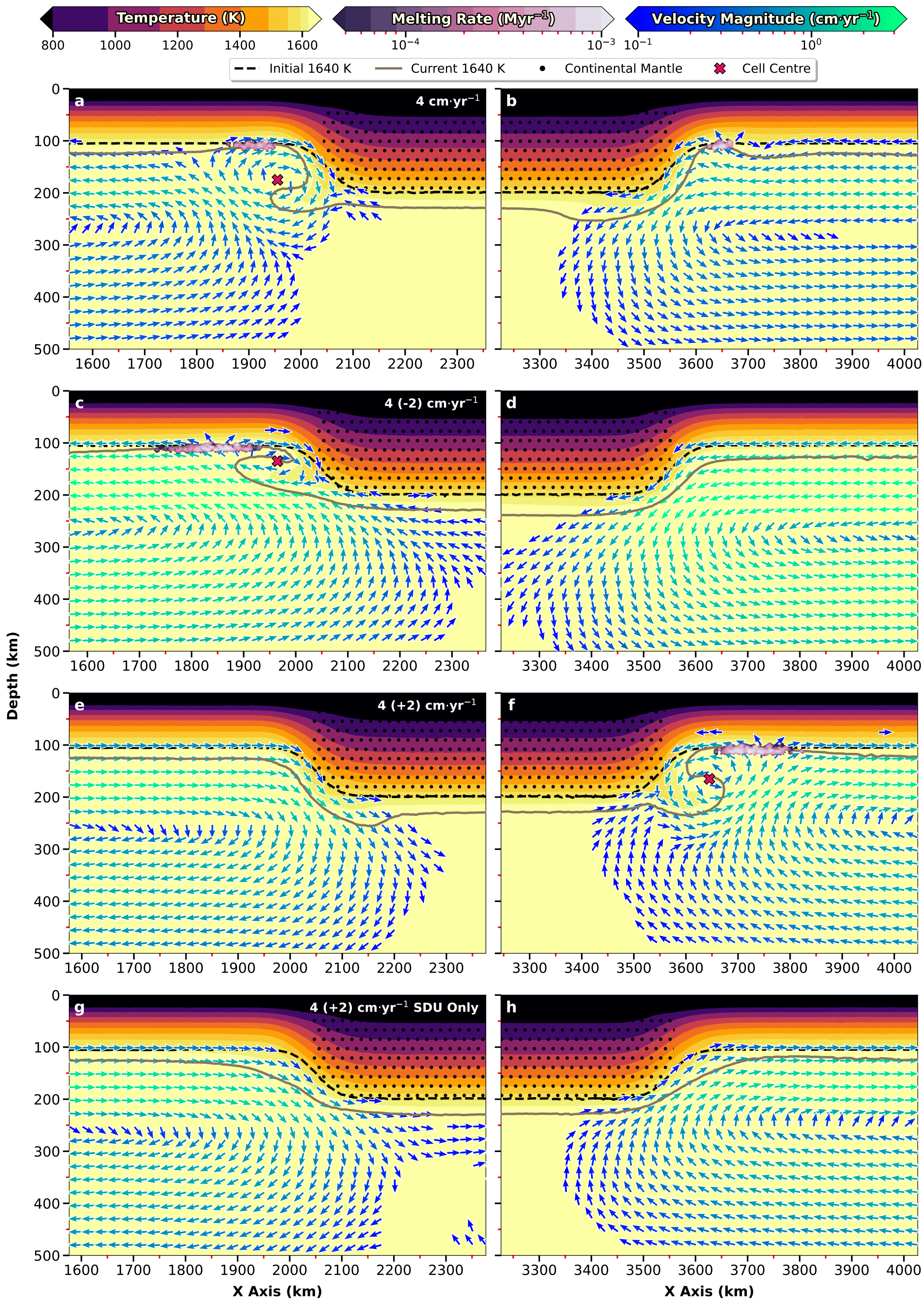

Figure 4. Effect of asthenospheric flow on edge-related dynamics. (a) & (b) $4\,\mathrm{cm\,yr^{-1}}$ purely plate-driven scenario. (c) & (d) A case with additional shear in the asthenosphere, directed opposite to plate motion. (e) & (f) Similar to (c) & (d), but with asthenospheric shear aligned with plate motion direction. (g) & (h) Similar to (e) & (f), but with the coefficient of thermal expansion set to 0, thus negating edge-driven instabilities. All models are displayed after 20 Myr of model evolution. Graphics illustration as in Figure 3, with the horizontal component of velocity relative to that of a vertical transect through the centre of the continent.

that of the profile beneath the centre of the continent (refer to Figure S3 for the full velocity field). In the purely plate-driven case (Figure 4a-b), the location of the 1640 K isotherm indicates that instabilities develop at both steps, although a clear cell is only identifiable adjacent to the left step. For this simulation, relative to the overlying plate, the Couette flow-component associated with plate motion (Figure S2) drives asthenospheric material to the left. As such, at the left step, the instability is displaced sideways, away from the step, and asthenospheric flow enhances the upwelling component of the edge-driven cell. Conversely, at the right step, asthenospheric motion acts against the cell, with the resulting downwelling driven horizontally below the continent. The differences between left and right steps increase in proportion to the magnitude of imposed plate motion, as reflected in Figure 5a-b where we plot the vertical component of velocity along a horizontal transect through the centre of each cell. These flow patterns explain why melting is enhanced at the left step relative to the right (quantified in Figure 6a-d and discussed further below).

Additional shear in the asthenosphere, in the direction opposite to plate motion (Figure 4c-d), increases the aforementioned contrast in behaviour between left and right steps. Under this scenario, both Couette and asthenospheric shear components act in the same direction, relative to the overlying plate. As such, at the left step, edge-driven convection, Couette flow and shear-driven flow combine to increase upwelling rates ('4 (-2)' curve on Figure 5a). We note that the style of upwelling is modified – upwelling flow becomes dominantly shear-driven, as reflected in the lateral displacement of the instability and the limited depth extent of the edge-driven cell. Regardless, melting is enhanced (both in intensity and spatial extent), with the melt region displaced away from the step. Conversely, at the right step, Couette and shear-driven flow combine to drive material beneath the continent, preventing upwelling (and melting) in this region.

The case where asthenospheric shear is aligned with the direction of plate motion incorporates counteracting flow regimes: at the left step, the Couette component of flow, associated with plate motion, acts to enhance the edge-driven cell, but the asthenospheric shear component acts to dampen it, with opposite trends at the right step. Nonetheless, as illustrated in Figure 4e-f, the asthenospheric shear component dominates on both steps, forcing material below the continent and shutting off melting at the left step, but increasing upwelling rates and melting adjacent to the right step. Interestingly, across the parameter space examined, the largest upwelling velocity recorded along the cell-centre transects (Figure 5) occurs for this specific model ('4 (+2)') where Couette and shear components of flow counteract. In this case, the edge-driven instability is able to develop more naturally: the drip descends more vertically and acquires a larger volume than in the '4 (-2)' case where flow components combine (compare Figure 4c with Figure 4f). We note that relative motion between continental lithosphere and underlying asthenosphere is far greater when they move in opposite directions (relative motion of $5\,\mathrm{cm\,yr^{-1}}$ in case '4 (-2)' compared to $1\,\mathrm{cm\,yr^{-1}}$ in case '4 (+2)', at 250 km depth – see Figure S2). As such, EDC is able to operate alongside asthenospheric shear in case '4 (+2)', rather than being completely dominated by it. Nevertheless, melting intensity is similar between these two cases, albeit occurring over a smaller spatial extent in case '4 (+2)'.

To further highlight the delicate balance between different flow components, we illustrate in Figure 4g-h the temperature and flow fields for a case identical to '4 (+2)', except that the coefficient of thermal expansion has been set to 0. As a result, temperature gradients no longer generate the density changes required to drive an edge instability at either step. Consequently, the shear-driven flow simply dives beneath the continent at the left step and rises at the right step. However, it is noteworthy that, during the first $\sim$7.5 Myr, maximum upwelling velocities at the right step are elevated compared to the case that incorporates buoyancy, indicating that the descending edge-driven instability partially counteracts shear-driven upwelling at this step (Figure S6). Over time, this situation reverses: upwelling velocities increase for the case that does incorporate

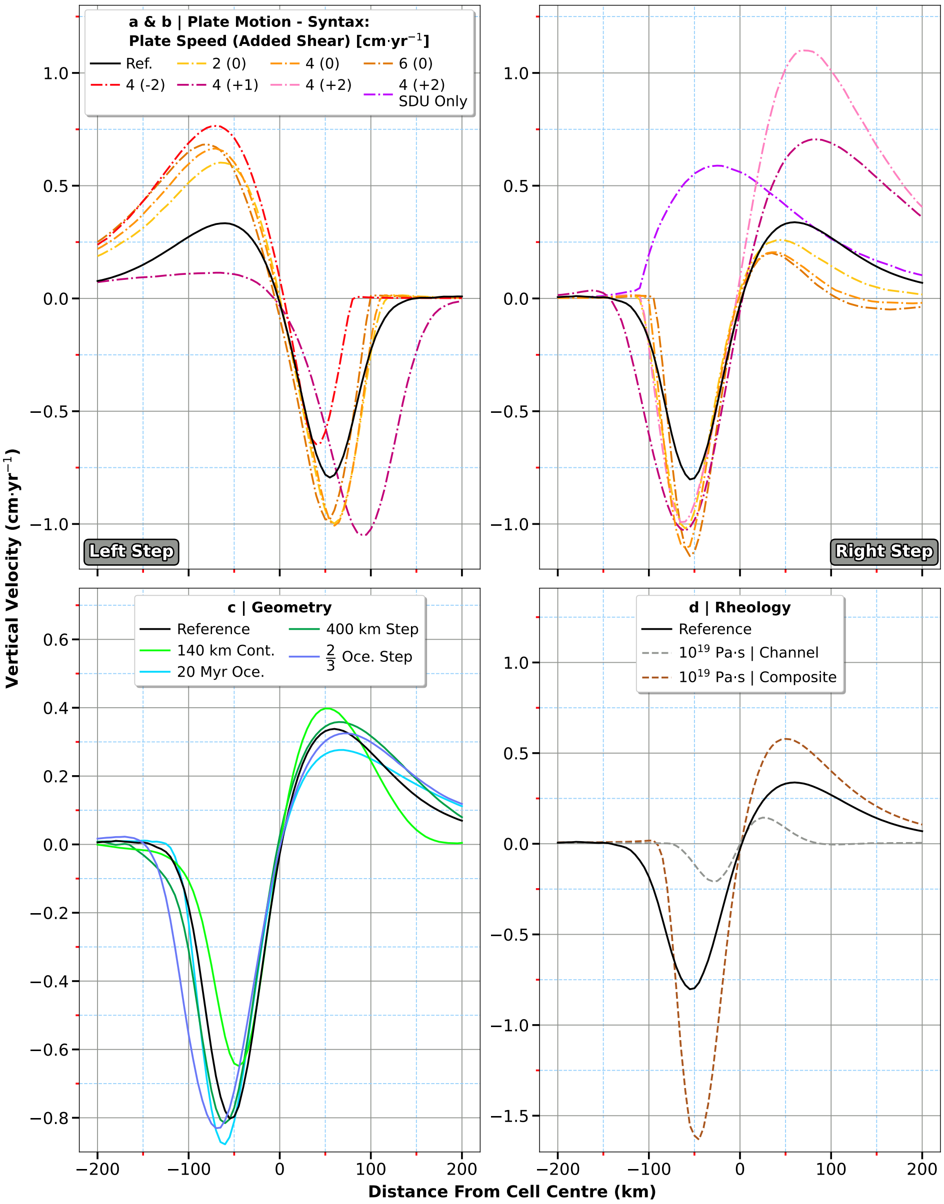

Figure 5. Comparison of vertical velocity in the vicinity of the cell centre (see Figure S4 for computed locations) at the right step (if not specified) for the 2-D simulations examined herein. As instabilities develop over different time-scales for different cases, we identify the centre of the cell in each simulation (Figure S4) at the time of maximum downwelling velocity (Figure S5), prior to the onset of secondary instabilities, to provide a meaningful comparison. Each profile represents a 400 km horizontal transect passing through the centre of the cell. (a) & (b) Influence of background asthenospheric flow – 'Reference' corresponds to an enclosed simulation. At the right step, purely plate-driven cases do not develop a full circulating cell and, accordingly, velocity profiles are displayed at depths picked to allow for illustration of upwelling velocities in a way that is comparable to other cases. Moreover, the case with SDU only does not generate a cell at all and we use the cell centre from the equivalent case ('4 (+2)') to draw the profile to allow for a representative comparison. (c) Effect of step geometry – 'Reference' corresponds to '40 Myr Oce.', '200 km Step', '200 km Cont.', and a material boundary halfway along the step. (d) Role of viscosity – 'Reference' corresponds to a purely diffusion creep channel-free profile with a minimum viscosity of 10^{19} Pa s.

buoyancy, as the instability grows, but upwelling velocities systematically decrease in the SDU-only case, as the upper thermal boundary layer thickens through diffusion, reducing the pressure difference between regions of thick and thin lithosphere. As a consequence, after ∼15 Myr, the lid has sufficiently thickened to prevent any decompression melting in the SDU-only case (Figure 6c). The interplay between buoyancy and mantle flow at lithospheric steps is further reflected in case '4 (+1)' (Figure 5a), for which asthenospheric shear is sufficient to counteract the Couette component of flow: horizontal flow within and just below the continent are of similar intensity (Figure S2). As a result, edge-driven instabilities develop akin to these of the reference case, and a weak cell is observed at the left step, despite it being strongly modulated by asthenospheric shear. Nevertheless, the presence of a weak cell enhances melting as it focusses upwelling velocities at shallower depths, closer to the solidus. Taken together, these results highlight that there is a threshold point at which EDC and SDU combine to maximise upwelling velocities adjacent to lithospheric steps. Where the shear-driven component is reduced, relative to this point, upwelling velocities decrease. Conversely, where the shear-driven component is increased, relative to this point, downwelling instabilities are unable to develop at lithospheric steps and, accordingly, the contribution from EDC is eliminated and upwelling is purely shear-driven.

We next compare the vigour of edge-driven instabilities across the remainder of our parameter space. Although we have examined a broad suite of models, we focus on representative end-members for clarity. As illustrated in Figure 5c, geometric parameters generally have only a moderate influence on the downwelling velocity, upwelling velocity and cell width (i.e. the distance between maximum downwelling and upwelling speeds along the profile) along these horizontal transects, with all profiles displaying similar characteristics. Nonetheless, in comparison to the reference case, the thinner continent ('140 km Cont.') yields a smaller cell, both in depth and lateral extent, with peak downwelling velocities reduced but peak upwelling velocities enhanced. Such differences arise primarily from the shorter continental guide at depth, which limits instability growth and downwelling velocities. As a result, flow circulation concentrates closer to the step and the extent of horizontal motion beneath the lithosphere decreases, facilitating an earlier onset of secondary instabilities. Accordingly, although peak upwelling velocities are initially smaller, they eventually overcome those of the reference case. In general, we find that increased space available along the continental guide (e.g. '20 Myr Oce.') and greater volumes of unstable oceanic lithosphere (e.g. '400 km Step' and '$\frac{2}{3}$ Oce. Step') lead to slightly stronger downwelling instabilities. Corresponding peak upwelling velocities, however, are not necessarily higher, but the lateral extent of the cells increases. In Figure 5d, we illustrate the important role of upper mantle viscosity and its depth-dependence. At a minimum viscosity of 10^{20} Pa s no comparable cell forms over the simulation times examined. The presence of a low-viscosity channel limits the vertical space over which an instability can develop and, accordingly, stabilises the lithosphere, reducing the intensity and scale of edge-driven instabilities. In the composite diffusion-dislocation creep regime, the intensity of the cell is enhanced, as a result of lower viscosities in the vicinity of the drip: a voluminous and focussed instability forms, generating a broad, robust upwelling (Figure S7).

To understand how these flow patterns influence melting, we present both instantaneous melting rates and cumulative melt diagnostics in Figure 6. Melting trends in cases with plate motion and asthenospheric shear are generally consistent with the flow fields highlighted above. For the first ∼20 Myr of model evolution, instantaneous melting rates are enhanced at the left step for cases with plate motion, and further enhanced when favourable asthenospheric shear is included. At the right step, plate-driven cases generate less melting than the reference case, but favourable asthenospheric shear once again enhances melt production. We note that a small amount of melting occurs at the left step for case '4 (+1)', as expected from the flow field highlighted above. For all cases with plate motion or asthenospheric shear, the onset of secondary instabilities is delayed and, hence, the

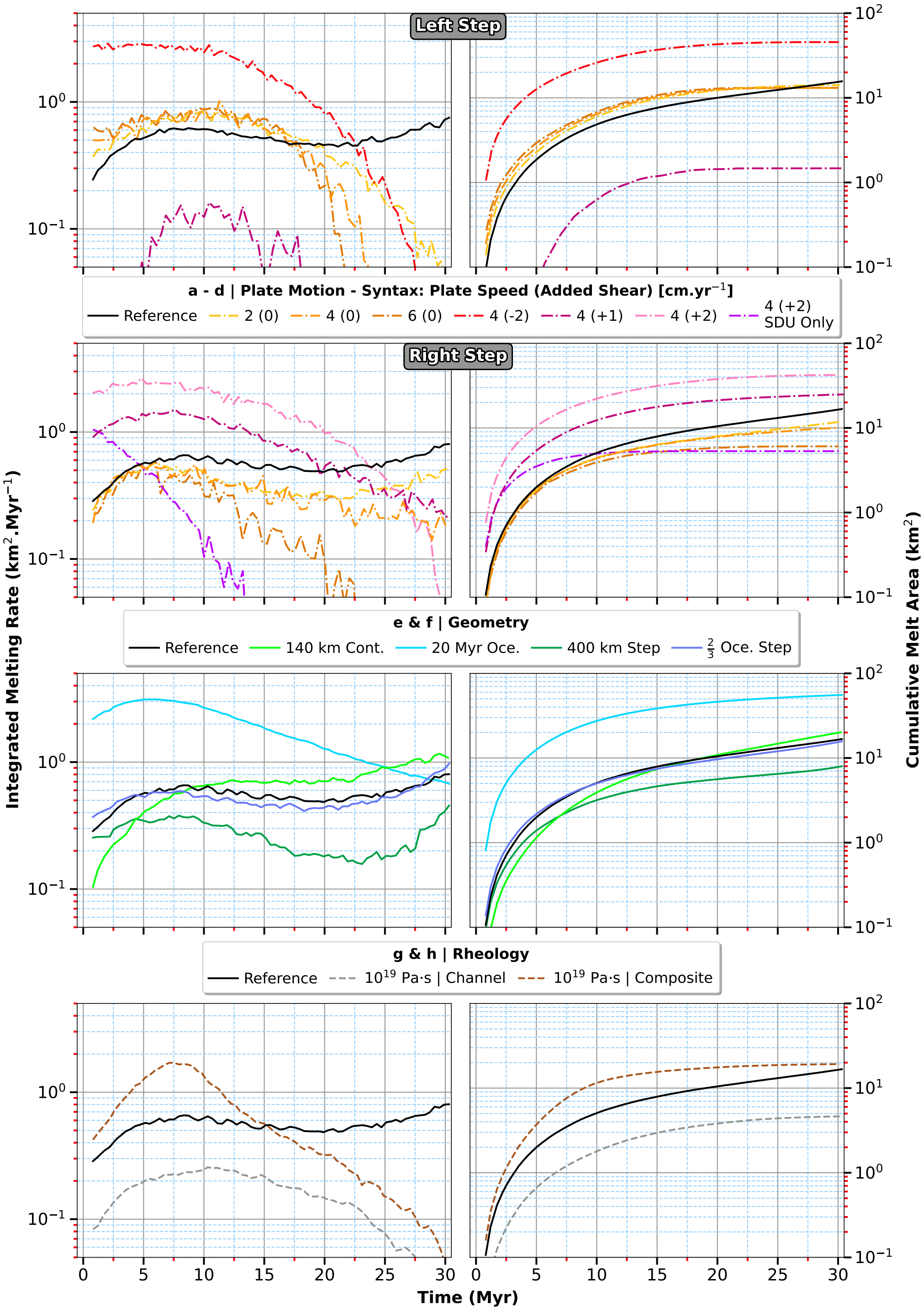

Figure 6. (a), (c), (e) & (g) Integrated melting rate measured at the right step (if not specified), as a function of time. Values correspond to the full integral in space of interpolated melting rates as recorded by particles. (b), (d), (f) & (h) Cumulative melt area, corresponding to the cumulative sum of melting rate additionally integrated in time. (a), (b), (c) & (d) Influence of asthenospheric flow – 'Reference' corresponds to an enclosed simulation. (e) & (f) Effect of step geometry – 'Reference' corresponds to '40 Myr Oce.', '200 km Step', '200 km Cont.', and a material boundary halfway along the step. (g) & (h) Role of viscosity – 'Reference' corresponds to a purely diffusion creep channel-free profile with a minimum viscosity of 10^{19} Pa s.

lithospheric lid thickens more rapidly than in cases without shear. As a consequence, instantaneous melting rates drop below the reference case beyond ∼20 Myr of model evolution – melting occurs over a shorter temporal duration for cases with a large component of asthenospheric shear. Such trends are further amplified in the absence of EDC, as illustrated by the SDU only case.

We find that most of the alternative step geometries analysed generate a comparable 'melt area' to that of the reference case, apart from the thinner lid ('20 Myr Oce') which enhances decompression melting (Figure 6e-f). Nonetheless, in the case of a wider step ('400 km Step'), melting rates are ∼50 % less than the reference case: the more gradual step generates a more-rounded cell, with upwelling flow less vertical at the LAB and, accordingly, less intense melting. Geometries such as '140 km Cont.' promote a more rapid onset of secondary instabilities, which thin the lithospheric lid and locally increase upwelling velocities. Such cases, therefore, initially display lower instantaneous melting rates, but eventually melt more than the reference case. Finally, cases with a minimum viscosity of 10^{20} Pa s exhibit no, or very limited, melting, whilst the incorporation of a low-viscosity channel reduces melting rates significantly, as expected from the aforementioned flow field (Figure 6g-h). In the composite viscosity regime, melting rates are higher for the first ∼15 Myr of model evolution. However, the broader and more intense cell delays the onset of secondary instabilities (due to increased shear beneath the lithosphere) and, thus, the cumulative melt curve flattens after ∼15 Myr, leading to a similar melt area to that of the reference case after 30 Myr.

3.2 Three-Dimensional Simulations

Our 2-D results highlight the importance of the orientation of asthenospheric shear in controlling the flow regime and associated melt production at lithospheric steps. Nonetheless, the 2-D geometry limits the range of scenarios that can be examined. Accordingly, we extend our analyses to 3-D, allowing for the incorporation of more complex geometries and greater flexibility in the orientation of asthenospheric flow. We separate our results into cases that neglect (Section 3.2.1) or incorporate (Section 3.2.2) background asthenospheric flow, respectively.

3.2.1 No Prescribed Asthenospheric Flow

We first examine the velocity field generated after 15 Myr: this is sufficient to capture the development of primary instabilities whilst avoiding complications linked to the onset of secondary instabilities, allowing us to focus upon 3-D effects that arise from more complex continental geometries. Nonetheless, for completeness, we illustrate through Figure S8, which is directly comparable to Figure 2, the development of secondary instabilities after 30 Myr in all 3-D geometries examined. Figure 7a displays the flow regime for Case U400, which exhibits edge-driven instabilities of comparable intensity adjacent to the entire continental boundary, except within the indent where darker red glyphs highlight more vigorous upwelling. At this location, the geometry of the interface between ocean and continent brings upwelling flows associated with three adjacent steps into close proximity: these coalesce (Figure S9a), enhancing upwelling velocities by as much as 70 % in comparison to those in other parts of the domain (Table 3).

Figure 7b displays results for Case U600. Although similar high-intensity upwelling velocities are present within the indent, they are restricted to the inner corners: in this case, the distance between edge-driven cells exceeds the width of the cells and, accordingly, cells on opposite steps are unable to coalesce and influence each other to the same extent as in Case U400 (Figure S9b). Figure 7c illustrates results from Case U400-Grad, with a complementary cross-section presented in Figure S10. Consistent with our 2-D cases (Figure 5c), downwelling velocities are enhanced adjacent to thicker parts of the continent, with upwellings broader and marginally less vigorous. Figure 7d illustrates

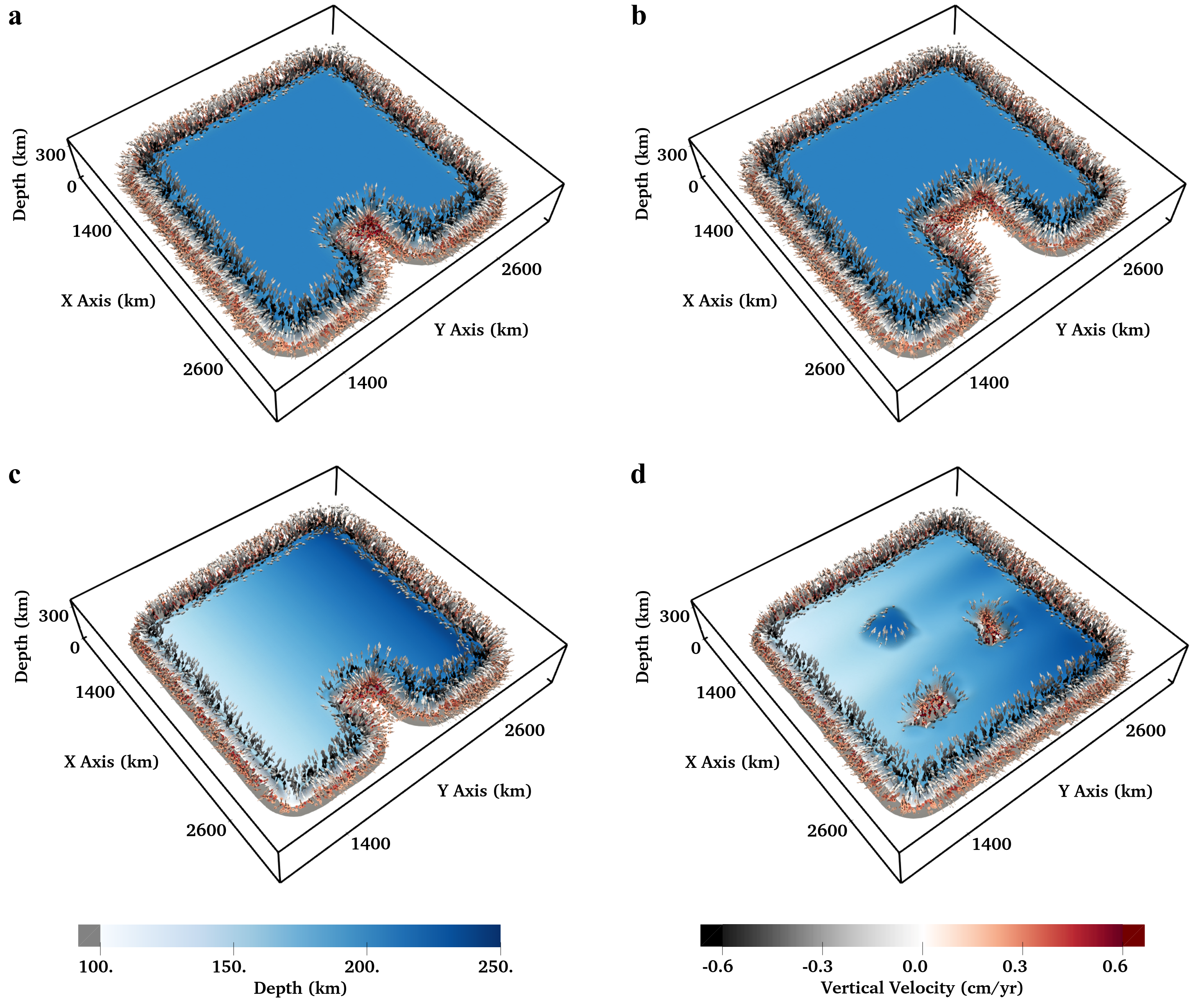

Figure 7. 3-D representation of the velocity field around the continent at 15 Myr, illustrated through a view looking at the base of the continent, from below. Surface colours correspond to the depth of the 1620 K isotherm – our proxy for lithospheric thickness – while arrow glyphs illustrate the velocity field. For visualisation purposes, glyphs are only drawn at locations where the velocity magnitude is larger than 2 mm yr^{-1}; glyphs all have the same length, are uniformly distributed and are coloured according to the vertical component of velocity. (a) Case U400. (b) Case U600. (c) Case U400-Grad. (d) Case Complex.

flow patterns for Case Complex and clearly demonstrates that regions of anomalously thin continental thickness trigger localised and strong upwelling flows. However, only moderate downwelling flows develop adjacent to the anomalously thick continental area: continental material resists deformation through its higher viscosity. Instabilities along continental boundaries are consistent with those in Case U400-Grad, as expected.

We now analyse the cumulative melt production for these cases. Results, presented in Figure 8, are expressed as a cumulative thickness, which results from the integration of melting rates both in time (over 15 Myr) and along the vertical axis (Section 2.4). Most melting occurs between 90 km and 120 km depth, consistent with the 2-D cases, except where the lithosphere is sufficiently thin to host shallower melting. For Case U400 (Figure 8a), we observe three distinct melting trends: (i) weak melting, adjacent to the external corners of the continent, producing less than ∼0.12 km of melt; (ii) moderate melting, at external steps away from the corners, producing up to ∼0.20 km of melt; and (iii) enhanced melting, within the indent, producing up to ∼0.45 km of melt, with the most intense melting concentrated at the indent's inner corners. Full spatial integration around the indent's lower-left corner (Figure 8a, 150 km-side black square) yields a cumulative volume of $\sim 3000\,\mathrm{km}^3$ distributed over an area of $\sim 15{,}600\,\mathrm{km}^2$ (Table 3). Melt fractions peak at 1 %, consistent with our 2-D cases. These trends are as expected from the intensity of upwelling at these locations.

In Figure 8b, we illustrate the spatial distribution of melt obtained for Case U600. We observe similar trends as for Case U400 and note, in particular, that comparable melting is recorded adjacent to the indent's inner corners, despite weaker flow coalescence (Figure S9), indicating that the geometry of the corners is sufficient to sustain melting. For Case U400-Grad (Figure 8c), steps adjacent to thicker parts of the continent generate around 30 % more melt than those adjacent to thinner parts, with a gradient in between, in agreement with Figure 6c – recall how the primary melting of '140 km Cont.', relative to our reference case, is initially reduced, but eventually enhanced through the action of secondary instabilities. Finally, for Case Complex (Figure 8d), trends at external steps are consistent with Case U400-Grad. Within the continent, significant melt-

Table 3. *Diagnostics Across 3-D Models*

Case	Maximum downwelling inside | outside indent ($\mathrm{cm\,yr^{-1}}$)	Maximum upwelling inside | outside indent ($\mathrm{cm\,yr^{-1}}$)	Maximum melt thickness[a] inside | outside indent (km)	Melt volume[b] (km^3) & area[c] (km^2) at the indent's corner
U400	−1.03 | −1.10	0.70 | 0.42	0.47 | 0.20	2976 & 15,594
U600	−1.01 | −1.11	0.67 | 0.42	0.47 | 0.20	2977 & 15,861
U400-Grad	−1.07 | −1.15	0.64 | 0.49	0.46 | 0.20	2951 & 15,850
Complex[d]	−0.61 | −1.17	0.87 | 0.48	0.70 | 0.20	3936 & 15,256
Pos. x	−0.97 | −1.40	1.31 | 0.84	0.66 | 0.33	5646 & 20,044
Neg. x	−1.13 | −1.41	0.39 | 0.92	0.21 | 0.35	837 & 7389
Pos. y	−1.19 | −1.37	1.11 | 0.91	0.60 | 0.33	4676 & 18,689
Oblique	−0.96 | −1.75	1.75 | 0.95	0.81 | 0.31	8103 & 21,080

[a] Cumulative thickness over the first 15 Myr of model evolution, obtained by integration of the melting rate carried by particles both in time and along the vertical axis (Figures 8 and 10). [b] Integration of the cumulative thickness in both x and y directions; only nodes (Section 2.4) with a cumulative thickness greater than 0.04 km and that are closest to the bottom-left inner corner of the indent (e.g. black square in Figure 8a) are considered. [c] Area defined by the nodes considered in the melt volume calculation. [d] For the first three columns, 'inside | outside the indent' is swapped for 'inside | outside the continent', while the last column 'indent's corner' is replaced by 'right trough' (black rectangle in Figure 8d).

ing is restricted to the two anomalous troughs, in agreement with the vigorous upwellings highlighted in Figure 7d. As a result of the initially thin continental lithosphere at these locations (60 km in places, as opposed to 90 km for surrounding oceanic lithosphere), we record up to 0.7 km of cumulative melt production, which is 50 % higher than observed at the indent's inner corners in Case U400. Additionally, melt volume within the right trough, recorded over a similar area (Table 3), is 30 % higher.

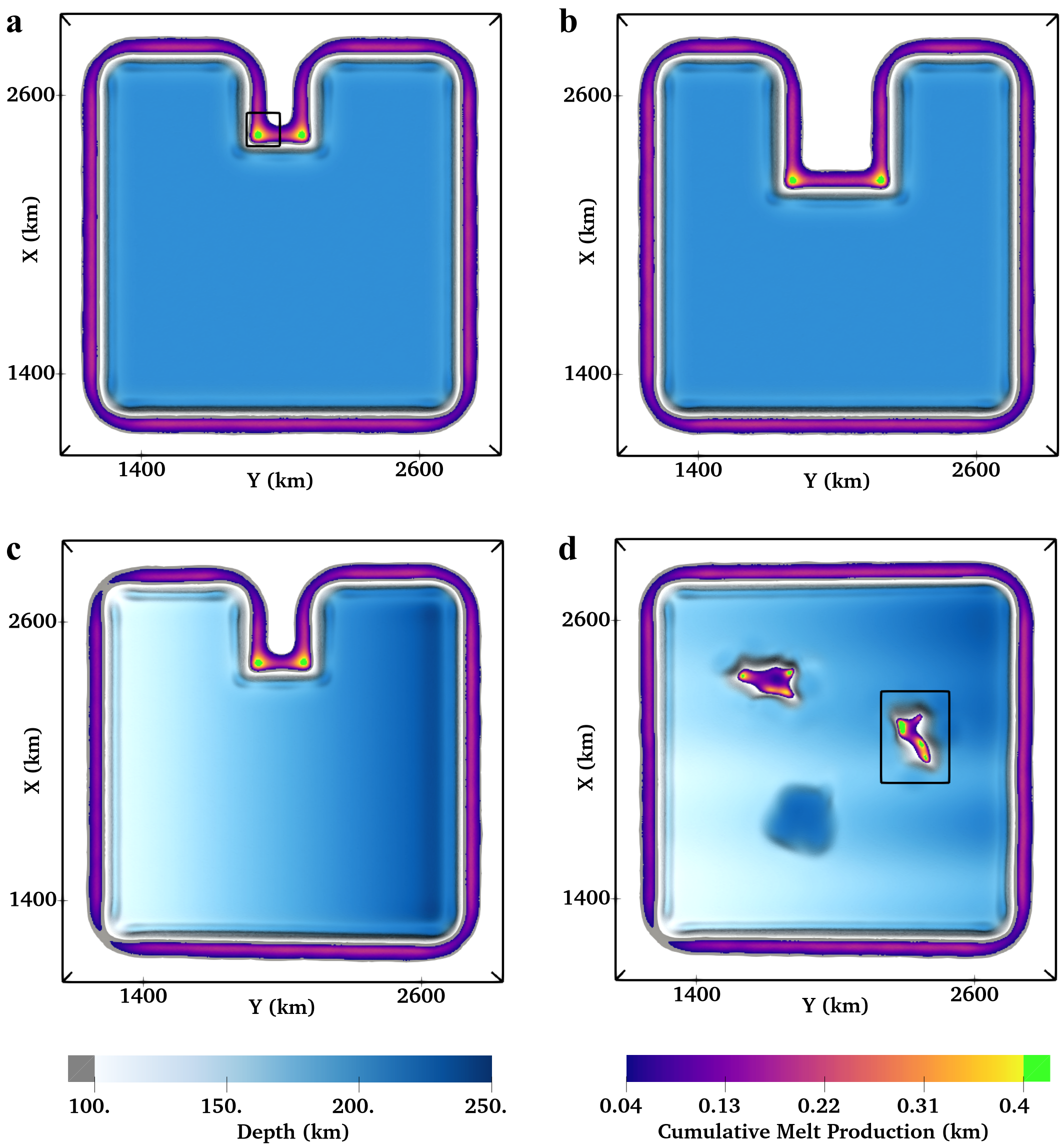

Figure 8. Cumulative melt production adjacent to the continent for cases without plate motion, after 15 Myr. Surface colours correspond to the depth of the 1620 K isotherm, our proxy for lithospheric depth; lithospheric erosion is identified by the grey tone, which depicts portions thinner than 100 km. Purple-to-yellow colours represent the cumulative melt production as obtained after integration along the vertical axis (Section 2.4); major locations of melting are indicated by the green tone. Black rectangles illustrate zones of interest used for calculations in Table 3. (a) Case U400. (b) Case U600. (c) Case U400-Grad. (d) Case Complex.

3.2.2 Prescribed Asthenospheric Flow

We next examine cases that incorporate prescribed asthenospheric flow and focus on how its orientation, relative to the continent, affects dynamical instabilities throughout the domain. We use Case U400 as our reference and systematically prescribe flow in the positive x, negative x, positive y, and both positive x and y (oblique) directions. We illustrate our results initially through the flow field (Figure 9) and, subsequently, through its influence on melting (Figures 10 and 11).

We find that velocities align with the prescribed inflow direction, in agreement with 2-D behaviour (Figure S3). Accordingly, to better highlight buoyancy-driven instabilities and allow for a consistent comparison with our 2-D cases, we modify the velocity field such that, at all depths, horizontal components are relative to those sampled on a vertical profile transecting through the centre of the continent. Figure 9a illustrates the resulting dynamics when asthenospheric shear is prescribed in the positive x-direction. Compared to Case U400 (Figure 7a), we observe enhanced upwelling velocities, increasing by up to $\sim$90 % inside the indent and $\sim$100 % where the asthenosphere flows away from the continent (i.e. the trailing edge). Conversely, where the asthenosphere flows toward the continent (i.e. the leading edge), upwelling velocities are reduced substantially by $\sim$70 %. The leading edge exhibits a clear downwelling, no associated upwelling, and divergent flow at continental corners. Conversely, intense upwelling takes place along the trailing edge and flow is convergent around the corners. Divergent and convergent flows at the continent's external corners occur due to the higher pressure beneath the continent, which drives material around continental margins and, accordingly, also contributes toward upwelling flow at the continent's lateral edges.

Figure 9b illustrates the flow field resulting from prescribed inflow in the negative x-direction. Trends are generally identical to the previous case on leading, trailing and outer lateral steps. However, upwelling velocities within the indent are no greater than those along the continent's lateral margins (Table 3): asthenospheric shear of this magnitude and orientation overcomes the dynamics of edge-driven convection imposed by the indent's geometric configuration. In Figure 9c, we illustrate the effect of incorporating shear in the positive y-direction. Both strong upwelling and downwelling velocities are observed within the indent (compared to Figure 7a), as the flow first upwells from below and then dives beneath the continent. Peak upwelling velocity is intermediate between Case U400 and the positive-x inflow case. For our oblique case (Figure 9d), the notion of leading and trailing edges evolves into the idea of pairs of edges adjacent to leading and trailing corners. Accordingly, downwellings concentrate alongside outer edges connected to the leading corner, whereas upwellings distribute adjacent to the opposite edges. Within the indent, we observe intense upward motion. Flow within the asthenosphere is favourably oriented to enhance upwellings at both steps adjacent to the lower-left inner corner (Figure 10d). Consequently, the vertical velocities recorded are the largest across all cases examined, a $\sim$250 % increase relative to Case U400.

We next analyse the cumulative melt production for these cases. In Figure 10a, we recover the three melting trends previously described for our reference 3-D case (Case U400). However, relative to the reference case, melting is absent at the continent's leading edge and enhanced at its trailing edge (by $\sim$65 %). Inside the indent, the maximum melt thickness increases by $\sim$40 % relative to Case U400, and melting takes place over a larger area, leading to a $\sim$90 % increase in local melt volume (Table 3). Inflow prescribed in the opposite direction (Figure 10b) yields similar trends at leading, trailing and lateral edges. In this case, melt production inside the indent is comparable to that observed at the continent's lateral edges and is less than that observed at the trailing edge. The calculated melt volume at the indent's lower-left corner falls to $\sim$840 km^3, equivalent to a $\sim$70 % decrease from Case U400. For inflow in the positive y-direction (Figure 10c), the distribution of melt production corresponds closely to locations of upwelling flow, especially within the indent where the recorded melt volume at the lower-left inner cor-

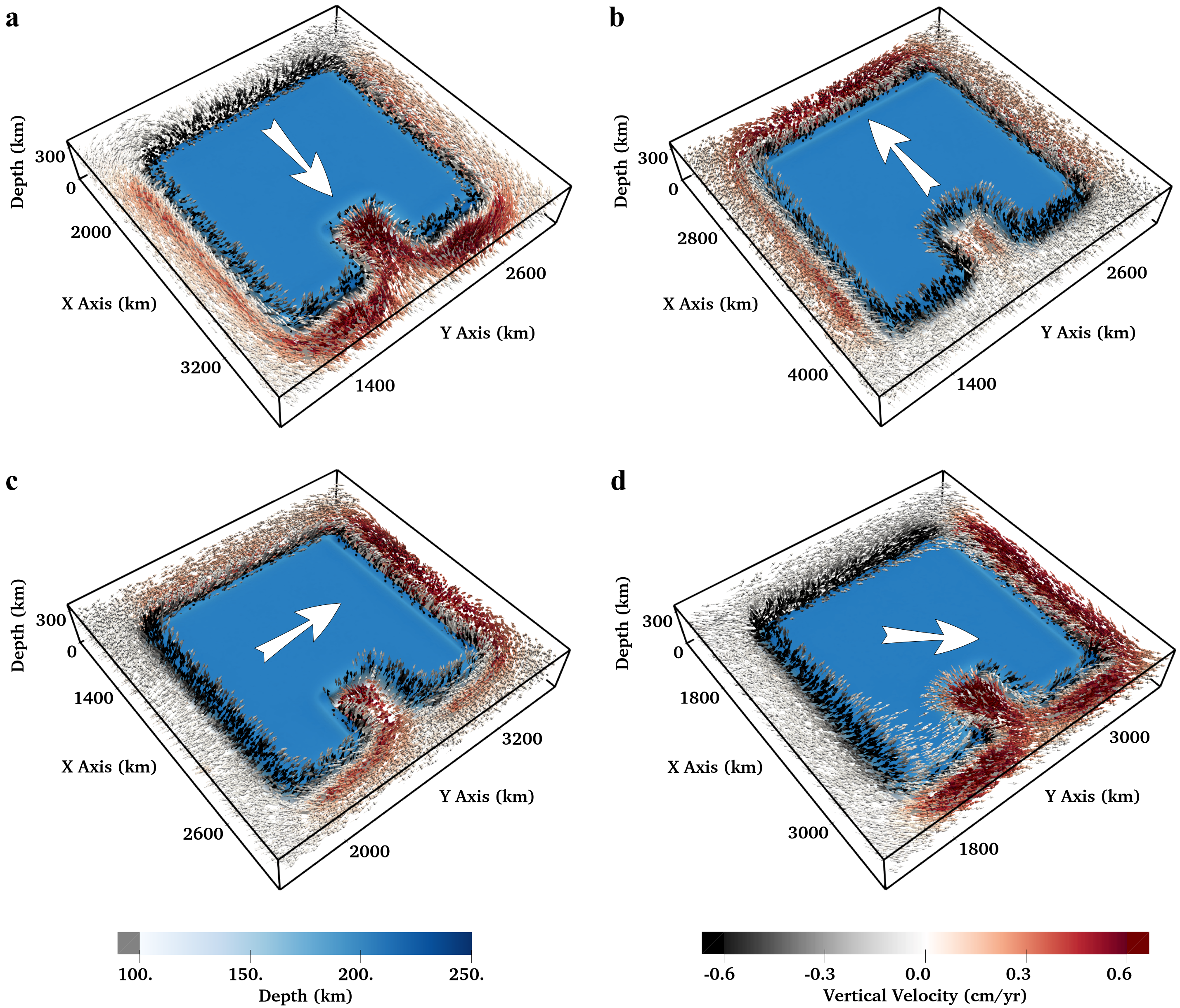

Figure 9. 3-D representation of the velocity field around the continental area after 15 Myr. Graphic illustration is similar to Figure 7; glyphs are only drawn where the velocity magnitude is greater than 4 mm yr^{-1}. Similar to Figure 4, horizontal components of velocity are relative to that sampled on the vertical profile centred through the continent, uncovering dynamical instabilities. Additionally, large white arrows represent both the direction of plate motion and the direction of asthenospheric flow relative to the continent, thereby pointing from the continent's leading edge to its trailing edge. (a) Prescribed flow in the direction of positive x. (b) Direction of negative x. (c) Direction of positive y. (d) Direction of both positive x and y.

ner represents ~80 % of that measured for the positive-x inflow. For our oblique case (Figure 10d), melting is absent at the pair of edges adjacent to the leading corner. At opposite edges, melt production is marginally lower than at a trailing edge experiencing purely normal flow (e.g. in the case of positive x-inflow) but still noticeably higher than at a comparable edge in the absence of asthenospheric flow (e.g. Case U400). As expected from the velocity field, a large area around the lower-left inner corner of the indent displays intense melt production, up to ~70 % higher than in Case U400. The calculated cumulative melt volume in this region is ~270 % higher than Case U400 and is the highest recorded across the parameter space examined.

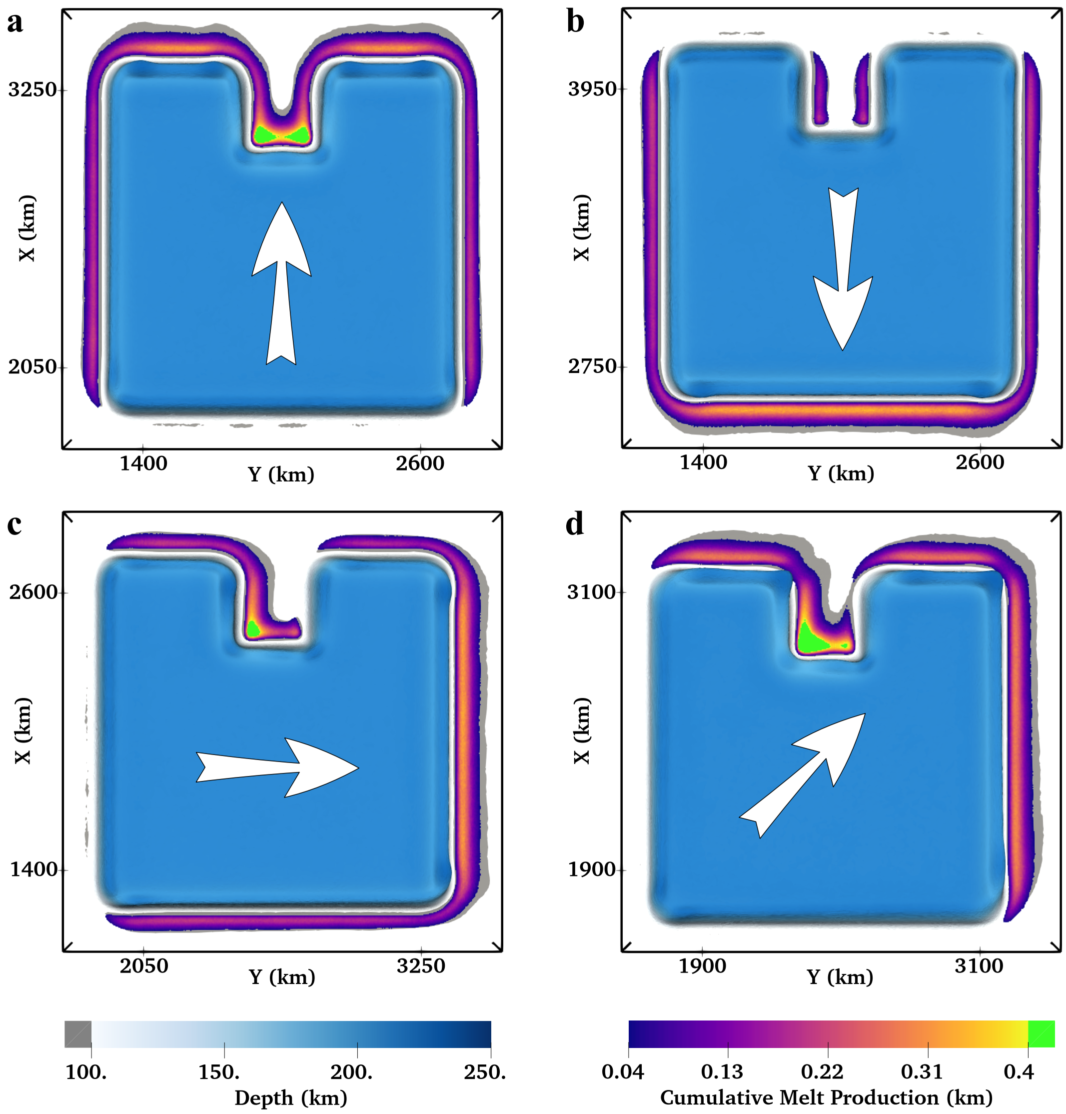

Figure 10. Cumulative melt production adjacent to the continent for cases with prescribed inflow, after 15 Myr. Graphic illustration is similar to Figure 8. Additionally, large white arrows represent both the direction of plate motion and the direction of asthenospheric flow relative to the continent, thereby pointing from the leading edge to the trailing edge. (a) Positive x. (b) Negative x. (c) Positive y. (d) Oblique.

Finally, we compare the spatial distribution of melts produced in our 3-D cases that incorporate asthenospheric flow (Figure 10) with Case U400 (Figure 8a). For each panel in Figure 10, we subtract the melt production from Figure 8a and illustrate the result in the corresponding panel of Figure 11. We make several important observations: (i) the leading edge of a continent is identified by a substantial decrease in melt production (dark pink colours) as material descends beneath the continent; (ii) trailing edges display an increase in melt production (green tones) as material rises from beneath the continent; (iii) lateral edges see no significant change in melt production; and (iv) the effect of flow direction is reflected in melting locations within the indent, with melting in-

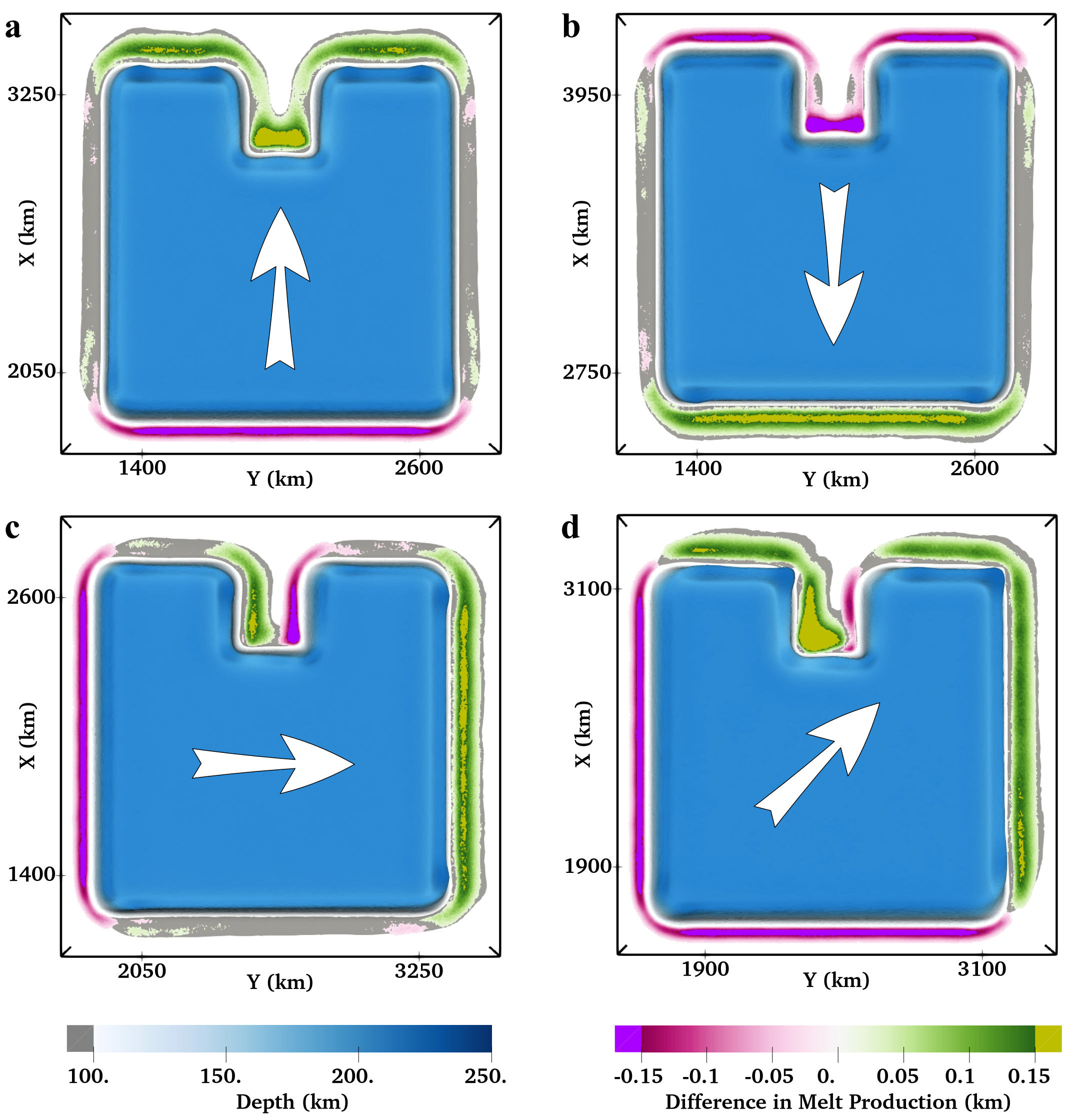

Figure 11. Relative production of melt between cases with prescribed inflow and Case U400. Each panel is generated as a difference between the corresponding panel in Figure 10 and Figure 8a; values in the range $-0.02\,\mathrm{km}$ to $0.02\,\mathrm{km}$ are not represented. Pink tones denote areas where melting is weakened by asthenospheric flow, while green tones highlight zones of enhanced melting. Large white arrows are consistent with Figure 10. (a) Positive x. (b) Negative x. (c) Positive y. (d) Oblique.

creasing significantly where interactions between upwelling currents are facilitated by the geometric configuration.

4 Discussion

We have quantitatively examined mantle flow and melt generation in the vicinity of lithospheric steps, using a suite of 2-D and 3-D numerical models. Our models reveal the dominant controls on edge-driven convection (EDC) and shear-driven upwelling (SDU), how these shallow processes interact, and under which conditions they can be linked to intra-plate volcanism.

We find that EDC is strongly sensitive to uppermost mantle viscosity and its depth dependence. At minimum viscosities $\geq 10^{20}$ Pa s, only weak edge-driven cells develop over the timescales of our simulations. If low viscosities are restricted to a narrow asthenospheric channel, the length-scale and vigour of edge-driven cells are reduced. These findings are consistent with several previous studies, which report that significant small-scale convection only develops at viscosities of less than 10^{19}-10^{20} Pa s (e.g. van Hunen et al., 2003; Currie et al., 2008; Le Voci et al., 2014; Davies et al., 2016). We find that the geometry and material properties of the step are also important in controlling EDC. Continental lithosphere guides downwelling flow and, thus, cases with deeper continental guides drive larger-scale cells. Other geometrical parameters, including the width of the step, the age (thickness) of oceanic lithosphere and the location of the interface between continent and ocean along the step, control the volume of lithospheric instabilities and, hence, the rate at which they develop and the vigour of the resulting cell. These findings build on those across a number of previous studies (e.g. Farrington et al., 2010; Till et al., 2010; Ballmer et al., 2011; Davies & Rawlinson, 2014; Kaislaniemi & van Hunen, 2014; Rawlinson et al., 2017).

By analysing EDC in the presence of plate-motion and asthenospheric shear, we have been able to shed light on how EDC and SDU interact. In 2-D, we find that Couette flow, induced by plate-motion, can enhance EDC where the asthenosphere flows away from the lithospheric step and suppress it where the asthenosphere flows toward the step. Depending upon its orientation, the addition of further asthenospheric shear can enhance or diminish the contrast in dynamics between leading and trailing continental edges. Where both processes combine, we find that melting is enhanced, even if the contribution from EDC is minimal. Under this scenario, EDC drives a small-scale upwelling at shallow depths, close to the step (e.g. Figure 4c), which enhances decompression melting. We emphasize that there is a threshold beyond which SDU dominates and EDC is suppressed: in our models with an imposed surface velocity, we find that EDC is largely overcome when relative motion between the continent and underlying asthenosphere exceeds $\sim 2\,\mathrm{cm\,yr^{-1}}$. At this stage, downwelling instabilities cannot drip vertically and are swept horizontally, with the morphology of upwelling flow also modified as a result. Although we have not undertaken an exhaustive parameter space study, we note that this threshold is sensitive to a number of parameters, including the geometry and material properties of the step, as well as uppermost mantle viscosity and its depth-dependence. Interestingly, as one approaches this threshold point, the negative buoyancy of lithospheric material at the step partially counteracts shear-driven upwelling: at times, upwelling velocities at depth are reduced in comparison to cases where buoyancy is not considered (Figure S6).

In 3-D, we find that the distribution of lithospheric steps and their relative orientation exert a key control on the system's dynamics: edge-driven cells at steps that are in close proximity can coalesce and, thereby, enhance and localise upwelling flow, with our models yielding upwelling velocities that are up to $\sim 70\,\%$ higher than would otherwise be the case – this corroborates the conclusions of Davies and Rawlinson (2014). In addition, cells are strongly sensitive to the orientation of background mantle flow. Consistent with our 2-D results, we find that edge-driven upwelling currents are strengthened through SDU where asthenospheric mantle flows away from the continent, but are suppressed where the asthenosphere flows toward the continent. Moreover, where asthenospheric flow is parallel to a lithospheric step, the modulation of edge-driven instabilities by asthenospheric shear does not strongly affect melting. We emphasise, however, that this may not be the case with more vigorous asthenospheric flow than examined herein. Our results demonstrate that, although lithospheric steps are an essential prerequisite for the development of edge-driven cells, the orientation and strength of asthenospheric flow determines whether or not these cells can form, their spatial extent and, ultimately, the location and degree of decompression melting. As an example, even though the structure of the indent is consistent across all 3-D cases examined, the orientation of the velocity field, relative to the continent, either promotes or impedes magmatism, leading to an order of magnitude variation in cumulative melt production at the indent's lower-left corner (Table 3).

The strong sensitivity of EDC and the associated melting to asthenospheric flow has important implications for our understanding of spatial and temporal patterns of intraplate volcanism at lithospheric steps. Importantly, our results imply that magmatism, generated in the presence of SDU, should be shorter-lived than that induced by EDC, given that increased shear at the LAB delays the development of secondary instabilities, which thin overlying lithosphere and, thus, prolong decompression melting. In addition, we find that magmatism induced by SDU is displaced further away from lithospheric steps, in the direction of asthenospheric shear. In Earth's vigorously convecting mantle, asthenospheric flow directions and magnitudes are likely to be time-dependent (e.g. Coltice et al., 2018; Iaffaldano et al., 2018; Coltice et al., 2019), with a strong sensitivity to changes in plate motion (e.g. Müller et al., 2016) and the shallow Poiseuille component of mantle flow (e.g. Phipps Morgan et al., 1995; Höink et al., 2011; Stotz et al., 2017, 2018). Our simulations suggest that these changes in asthenospheric flow directions and magnitudes will strongly modulate edge-driven cells and the associated magmatism. To illustrate this further, in Figure S11 we present results from an additional 3-D simulation, where the direction of plate motion and asthenospheric shear is rotated by 90° after 16 Myr. Under such a scenario, edge-driven flow and the associated magmatism could be enhanced, reduced or even suppressed, within only a few million years of the plate motion change, at any given location along a lithospheric step. In particular, an edge that was originally orientated parallel to asthenospheric mantle flow records a clear and substantial increase (decrease) in melt production as it has transitioned to a trailing (leading) edge. We note that these trends are visible in our melting diagnostics within only a few million years of the plate motion change (Figure S11b-c). It is noteworthy that the original leading edge does not display a substantial increase in melt production following the plate motion change, suggesting a longer lag for steps dominated by downwelling currents prior to a change in the asthenospheric flow direction, thus pointing towards a history dependence in the system. The history of mantle flow, therefore, becomes important to understanding why specific locations generate magmatic trends that deviate from their expected behaviour based upon present-day estimates of lithospheric geometries, plate motion and asthenospheric flow directions. This reinforces the notion that volcanic provinces likely controlled by EDC and SDU will be comparatively short lived and time-dependent. We note that these mechanisms are in addition to those identified in previous studies that lead to a periodicity in edge-driven melting (e.g. Kaislaniemi & van Hunen, 2014).

Our study builds on and complements previous studies, for example, Till et al. (2010) and Davies and Rawlinson (2014), by (i) examining the interaction between EDC and asthenospheric shear over a wider range of asthenospheric flow intensities, distributions and orientations; (ii) examining more complex lithospheric structures and step geometries in 3-D, which allow for the coalescence and localisation of upwelling; (iii) incorporating an improved treatment of mantle melting that accounts for melt history using Lagrangian particles; and (iv) accounting for the time-dependence of these systems, which differs from the instantaneous flow models of Davies and Rawlinson (2014). Nonetheless, consistent with these, and other, studies, our results support EDC and SDU as viable mechanisms for intra-plate volcanism in the vicinity of lithospheric steps, particularly where the geometry, material properties and orientation of these steps, relative to each other and asthenospheric mantle flow, are favourable. Over 15 Myr of model evolution, our simulations neglecting the role of asthenospheric shear predict melt thicknesses of up to 0.20 km adjacent to continental margins, up to 0.47 km at an indent's inner corner, and 0.70 km inside the anomalous continental trough of our more complex LAB case (Table 3). When asthenospheric flow is incorporated, trailing edges, where the asthenosphere flows away from the continent, record up to 0.35 km, while production at the indent's inner corners increases up to 0.81 km. Although melt volumes recorded adjacent to the indent's inner corners are reasonably consistent for all cases that neglect asthenospheric flow ($\sim$3000 km^3), they are strongly modulated by the orientation of asthenospheric flow when it is present: up to $\sim$8100 km^3, within an area of $\sim$21,100 km^2 (Table 3), is predicted for the 3-D oblique case over 15 Myr of model evolution. Such a volume corresponds to a mean magmatic production rate of $\sim$0.54 km^3 kyr^{-1}. We note that these rates are further modulated by secondary instabilities.

Our predicted melt volumes and melting rates suggest that, in isolation, EDC and SDU are suitable mechanisms only for Earth's lower-volume intra-plate volcanic provinces. Taking into account the sensitivity of melting to the thickness of the overlying lid (Figure 6c), the composition and water content of upper-mantle rocks, in addition to the potential impact of rheological uncertainties in our models (as indicated by different melting rates in our diffusion versus composite viscosity models), our results suggest that EDC

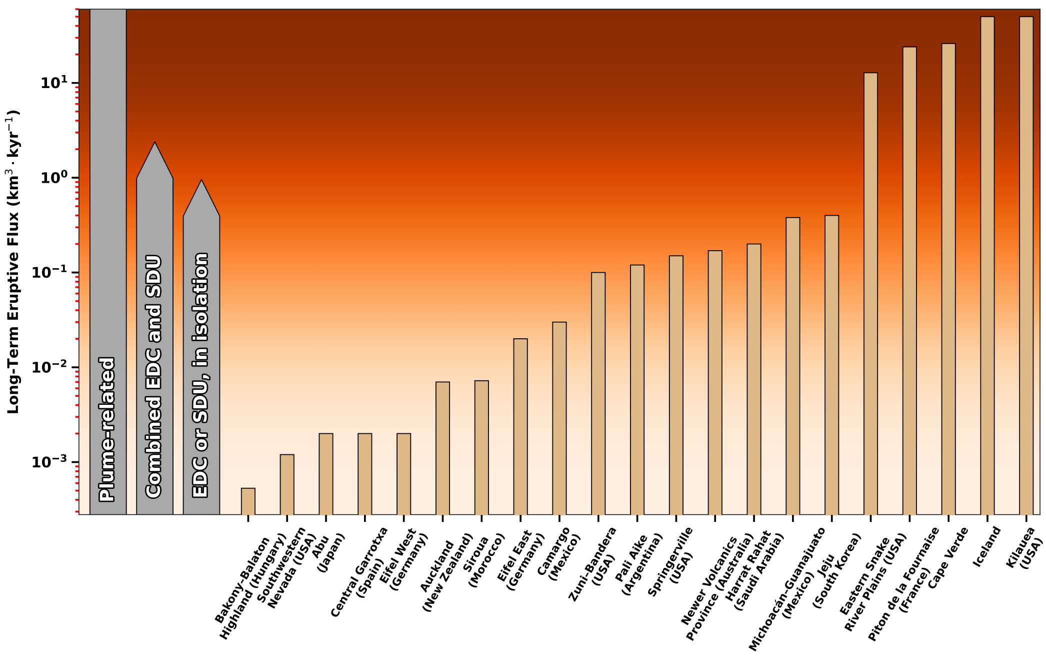

Figure 12. Long-term eruptive flux for a selection of intra-plate volcanic fields (building on van den Hove et al., 2017). Vertical grey arrows indicate the expected long-term flux that can be accounted for by given melt-generating mechanisms; we infer that mantle plumes are required to explain the largest fluxes observed. Values for province fluxes are taken from van den Hove et al. (2017), or as follows: Kilauea (Dvorak & Dzurisin, 1993), Iceland (Thordarson & Höskuldsson, 2008), Piton de la Fournaise (Roult et al., 2012), Cape Verde (Holm et al., 2008), Siroua (Missenard & Cadoux, 2012).

or SDU, in isolation, can account for magmatic production rates of up to $\sim 1\,\mathrm{km^3\,kyr^{-1}}$, whilst EDC enhanced by SDU should sustain up to $\sim 2.5\,\mathrm{km^3\,kyr^{-1}}$, the latter value being a simple $\times 2.5$ increase as deduced from Table 3. Accordingly, such shallow processes cannot explain, for example, eruptive rates at Earth's largest intra-plate volcanic provinces, including the Hawaiian Ridge, Iceland, Reunion and Cape Verde, where effusion rates exceed $10\,\mathrm{km^3\,kyr^{-1}}$ (e.g. Dvorak & Dzurisin, 1993; Thordarson & Höskuldsson, 2008; Holm et al., 2008; Roult et al., 2012). However, as illustrated in Figure 12, the magmatic rates predicted herein are comparable to those determined from field observations at a number of Earth's smaller intra-plate volcanic provinces, including the Newer Volcanics Province of Victoria and South Australia, the old Springerville volcanic field within the Southern Colorado Plateau, and the Siroua volcanic field of the Morrocan Atlas Mountains, all of which lie in close proximity to step-changes in lithospheric thickness and exhibit a long-term eruptive flux smaller than $0.2\,\mathrm{km^3\,kyr^{-1}}$ (e.g. Condit et al., 1989; Missenard & Cadoux, 2012; van den Hove et al., 2017; Cas et al., 2017).

It is important to emphasise that such comparisons should be nuanced and are indicative only. Firstly, our models yield magmatic fluxes at depth, whereas observations focus on eruptive fluxes at the surface. In addition, many of our chosen model parameters may not be appropriate at a given location. For example, in our 3-D simulations, we set the initial depth of oceanic lithosphere to $\sim 90\,\mathrm{km}$, which increases over time through thermal diffusion – most of the aforementioned provinces are located above thinner lithosphere, which would increase predicted melting rates and volumes (e.g. Davies & Rawlinson, 2014; Priestley et al., 2018). Furthermore, all numerical models have limitations, and some of our model assumptions may influence results. In particular:

1. In our melting calculations, for simplicity, we assume a peridotitic composition – magmatism may be locally enhanced (or reduced) through the presence of more enriched (or depleted) compositions. Furthermore, we assume a wet peridotite batch melting parameterisation and make no attempt to simulate the dynamics of melt transport and extraction. Whilst melt extraction has been considered in other modelling studies (e.g. Ballmer et al., 2011; Jain et al., 2019), the strategies used to model this process remain under development, particularly in the context of single-phase Stokes flow.
2. Although our models capture the effect of latent heating, they do not include direct feedbacks between melting and key material properties, such as density and viscosity. The low melting rates observed in our simulations, however, suggest that such feedbacks will have only a minor impact on our model predictions.
3. We model the continent as a rigid and viscous block, that is not dramatically impacted by edge-driven processes. It is possible that parts of the continental edge behave weakly, modifying the edge-driven process and associated melting (e.g. Liu & Chen, 2019).
4. Our study has focused on simulations with short evolution times, to isolate the sensitivity of EDC and SDU to the controlling parameters examined. In reality, lithospheric steps, particularly those at cratonic margins, are likely long-lived (e.g. Hoggard et al., 2020). Simulations with longer evolution times develop secondary instabilities that make it more challenging to isolate the signals highlighted herein. However, as illustrated in Figure S12 which compares both flow dynamics and melting patterns for Case U400 after 15 Myr and 30 Myr, the first order trends that we predict should remain consistent, with melting enhanced within the indent relative to external steps.
5. The strength and scale of edge-driven cells in our simulations is strongly dependent on the magnitude and depth-dependence of viscosity, which remain uncertain (e.g. Korenaga & Karato, 2008; Paulson & Richards, 2009; Iaffaldano & Lambeck, 2014; Rudolph et al., 2015). Nonetheless, we have examined the sensitivity

of our results under a range of different scenarios, all of which are within the estimated range (e.g. Iaffaldano & Lambeck, 2014; Lau et al., 2016).

6. We neglect other important aspects of mantle convection, including compressibility, phase transitions, global mantle flow and the impact of mantle plumes (e.g. Tackley et al., 1993; Gassmöller et al., 2020).

Each of these points requires further investigation to quantify their effect on the flow field and associated melting diagnostics. Nonetheless, our results suggest that EDC and SDU are capable of generating magmatic rates of 0.1-2.5 $\mathrm{km}^3\,\mathrm{kyr}^{-1}$ under favourable conditions. As illustrated in Figure 12, this is compatible with eruptive rates determined for a number of intra-plate volcanic provinces on Earth that lie adjacent to step-changes in lithospheric thickness, supporting EDC and SDU as viable mechanisms. At other provinces, where substantially enhanced melting rates are measured, alternative mechanisms, such as mantle plumes, are likely more applicable. Additionally, there is increasing evidence that the shallow mechanisms examined herein interact with upwelling mantle plumes at some locations to produce complex volcanic patterns at the surface (e.g. Davies et al., 2015; Rawlinson et al., 2017; Kennett & Davies, 2020). Understanding these interactions is an important avenue for future research.

5 Conclusion

This study systematically documents the behaviour of EDC and SDU in 2-D and 3-D geodynamical models. Our 2-D simulations demonstrate that EDC, which results from the negative buoyancy of lithospheric mantle adjacent to a rigid continental block at a lithospheric step, is sensitive to the geometry and material properties of that step, in addition to the upper mantle viscosity profile – given sufficient space, EDC cells can develop at viscosities below 10^{20} Pa s. Furthermore, we have highlighted how EDC can be enhanced, suppressed or, under certain conditions, completely eclipsed by SDU.

By examining the interaction between EDC and SDU in 3-D, we have demonstrated that edge-driven cells developing at adjacent lithospheric steps can modulate each other to enhance and localise upwelling. Additionally, flow in the asthenosphere can either intensify or weaken edge-driven upwellings, depending on the intensity of asthenospheric currents and their orientation relative to the moving continent. In our models, these flow patterns control the observed melting trends: increased melting occurs at locations of intense upwelling. Our predicted melt volumes suggest that, in the absence of potential interactions with mantle plumes, EDC and SDU are viable mechanisms only for Earth's shorter-lived and lower-volume intra-plate volcanic provinces. Altogether, our results illustrate the importance of local variations in lithospheric thickness and the orientation and magnitude of asthenospheric flow in controlling the location and timing of EDC and SDU-generated intra-plate volcanism. Most importantly, although changes in lithospheric thickness provide a favourable setting for EDC, edge-driven cells can be enhanced, displaced or overwhelmed by asthenospheric flow. As such, our study helps to explain why step changes in lithospheric thickness, which are common along cratonic edges and passive margins, only produce volcanism at isolated points in space and time.

Acknowledgments

T.D. is funded by an ANU PhD Scholarship (International) Full-Time (737/2018). D.R.D. acknowledges support from the Australian Research Council (ARC), under FT140101262. C.R.M is funded by an Australian Government Research Training Program Domestic Scholarship. D.R.D., S.C.K. and T.D. acknowledge support from the ARC under DP170100058. Numerical simulations were undertaken on the NCI National Facility in Canberra, Australia, which is supported by the Australian Commonwealth Government. The Fluidity computational modelling framework, including source code and documentation, is available from `https://fluidityproject.github.io/`; the latest release (tag 4.1.18), which was used for the simulations presented herein, has been archived at Zenodo (Kramer et al., 2021). Similarly, example input files required to reproduce the simulations presented herein have been made available (Duvernay, 2021). The authors are grateful to two anonymous reviewers for their constructive and detailed comments, which led to significant improvements in the manuscript. Additionally, we would like to thank Patrick Ball, Brian Kennett, Ian Campbell, Nick Rawlinson, Caroline Eakin, Marthe Klöcking, Siavash Ghelichkan and Cian Wilson for fruitful discussions at various stages of this research. Figures have been prepared using Matplotlib, ParaView and Inkscape.

References

Afonso, J. C., Rawlinson, N., Yang, Y., Schutt, D. L., Jones, A. G., Fullea, J., & Griffin, W. L. (2016). 3-D multiobservable probabilistic inversion for the compositional and thermal structure of the lithosphere and upper mantle: III. Thermochemical tomography in the Western-Central US. *Journal of Geophysical Research: Solid Earth*, *121*(10), 7337–7370.

Artemieva, I. M. (2009). The continental lithosphere: reconciling thermal, seismic, and petrologic data. *Lithos*, *109*(1-2), 23–46.

Ballmer, M. D., Conrad, C. P., Smith, E. I., & Johnsen, R. (2015). Intraplate volcanism at the edges of the Colorado Plateau sustained by a combination of triggered edge-driven convection and shear-driven upwelling. *Geochemistry, Geophysics, Geosystems*, *16*(2), 366–379.

Ballmer, M. D., Ito, G., Van Hunen, J., & Tackley, P. J. (2011). Spatial and temporal variability in Hawaiian hotspot volcanism induced by small-scale convection. *Nature Geoscience*, *4*(7), 457–460.

Bianco, T. A., Conrad, C. P., & Smith, E. I. (2011). Time dependence of intraplate volcanism caused by shear-driven upwelling of low-viscosity regions within the asthenosphere. *Journal of Geophysical Research: Solid Earth*, *116*(B11).

Bredow, E., Steinberger, B., Gassmöller, R., & Dannberg, J. (2017). How plume-ridge interaction shapes the crustal thickness pattern of the Réunion hotspot track. *Geochemistry, Geophysics, Geosystems*, *18*(8), 2930–2948.

Brent, R. P. (2013). *Algorithms for minimization without derivatives.* Courier Corporation.

Buck, W. R. (1986). Small-scale convection induced by passive rifting: the cause for uplift of rift shoulders. *Earth and Planetary Science Letters*, *77*(3-4), 362–372.

Cas, R., Van Otterloo, J., Blaikie, T., & Van Den Hove, J. (2017). The dynamics of a very large intra-plate continental basaltic volcanic province, the Newer Volcanics Province, SE Australia, and implications for other provinces. *Geological Society, London, Special Publications*, *446*(1), 123–172.

Coltice, N., Husson, L., Faccenna, C., & Arnould, M. (2019). What drives tectonic plates? *Science advances*, *5*(10), eaax4295.

Coltice, N., Larrouturou, G., Debayle, E., & Garnero, E. J. (2018). Interactions of scales of convection in the Earth's mantle. *Tectonophysics*, *746*, 669–677.

Condit, C. D., Crumpler, L., Aubele, J. C., & Elston, W. E. (1989). Patterns of volcanism along the southern margin of the Colorado Plateau: The Springerville field. *Journal of Geophysical Research: Solid Earth*, *94*(B6), 7975–7986.

Conrad, C. P., Bianco, T. A., Smith, E. I., & Wessel, P. (2011). Patterns of intraplate volcanism controlled by asthenospheric shear. *Nature Geoscience*, *4*(5), 317–321.

Conrad, C. P., Wu, B., Smith, E. I., Bianco, T. A., & Tibbetts, A. (2010). Shear-driven upwelling induced by lateral viscosity variations and asthenospheric shear: A mechanism for intraplate volcanism. *Physics of the Earth and Planetary Interiors*, *178*(3-4), 162–175.

Courtillot, V., Davaille, A., Besse, J., & Stock, J. (2003). Three distinct types of hotspots in the Earth's mantle. *Earth and Planetary Science Letters*, *205*(3-4),

295–308.
Currie, C. A., Huismans, R. S., & Beaumont, C. (2008). Thinning of continental backarc lithosphere by flow-induced gravitational instability. *Earth and Planetary Science Letters*, *269*(3-4), 436–447.
Currie, C. A., & van Wijk, J. (2016). How craton margins are preserved: Insights from geodynamic models. *Journal of Geodynamics*, *100*, 144–158.
Davies, D. R., & Davies, J. H. (2009). Thermally-driven mantle plumes reconcile multiple hot-spot observations. *Earth and Planetary Science Letters*, *278*(1-2), 50–54.
Davies, D. R., Davies, J. H., Hassan, O., Morgan, K., & Nithiarasu, P. (2007). Investigations into the applicability of adaptive finite element methods to two-dimensional infinite Prandtl number thermal and thermochemical convection. *Geochemistry, Geophysics, Geosystems*, *8*(5).
Davies, D. R., Le Voci, G., Goes, S., Kramer, S. C., & Wilson, C. R. (2016). The mantle wedge's transient 3-D flow regime and thermal structure. *Geochemistry, Geophysics, Geosystems*, *17*(1), 78–100.
Davies, D. R., & Rawlinson, N. (2014). On the origin of recent intraplate volcanism in Australia. *Geology*, *42*(12), 1031–1034.
Davies, D. R., Rawlinson, N., Iaffaldano, G., & Campbell, I. H. (2015). Lithospheric controls on magma composition along Earth's longest continental hotspot track. *Nature*, *525*(7570), 511–514.
Davies, D. R., Wilson, C. R., & Kramer, S. C. (2011). Fluidity: A fully unstructured anisotropic adaptive mesh computational modeling framework for geodynamics. *Geochemistry, Geophysics, Geosystems*, *12*(6).
Demidjuk, Z., Turner, S., Sandiford, M., George, R., Foden, J., & Etheridge, M. (2007). U-series isotope and geodynamic constraints on mantle melting processes beneath the Newer Volcanic Province in South Australia. *Earth and Planetary Science Letters*, *261*(3), 517–533.
Duncan, R. A., & Richards, M. (1991). Hotspots, mantle plumes, flood basalts, and true polar wander. *Reviews of Geophysics*, *29*(1), 31–50.
Duvernay, T. (2021). *Patol75/Linking-Intra-Plate-Volcanism-to-Lithospheric-Structure-and-Asthenospheric-Flow: Submission to Geochemistry, Geophysics, Geosystems.* Zenodo. Retrieved from `https://doi.org/10.5281/zenodo.4896782` doi: 10.5281/zenodo.4896782
Dvorak, J. J., & Dzurisin, D. (1993). Variations in magma supply rate at Kilauea Volcano, Hawaii. *Journal of Geophysical Research: Solid Earth*, *98*(B12), 22255–22268.
Farnetani, C. G., & Richards, M. A. (1995). Thermal entrainment and melting in mantle plumes. *Earth and Planetary Science Letters*, *136*(3-4), 251–267.
Farrington, R., Stegman, D., Moresi, L., Sandiford, M., & May, D. (2010). Interactions of 3D mantle flow and continental lithosphere near passive margins. *Tectonophysics*, *483*(1-2), 20–28.
French, S. W., & Romanowicz, B. (2015). Broad plumes rooted at the base of the Earth's mantle beneath major hotspots. *Nature*, *525*(7567), 95.
Garel, F., Goes, S., Davies, D. R., Davies, J. H., Kramer, S. C., & Wilson, C. R. (2014). Interaction of subducted slabs with the mantle transition-zone: A regime diagram from 2-D thermo-mechanical models with a mobile trench and an overriding plate. *Geochemistry, Geophysics, Geosystems*, *15*(5), 1739–1765.
Gassmöller, R., Dannberg, J., Bangerth, W., Heister, T., & Myhill, R. (2020). On formulations of compressible mantle convection. *Geophysical Journal International*, *221*(2), 1264–1280.
Gibert, B., Seipold, U., Tommasi, A., & Mainprice, D. (2003). Thermal diffusivity of upper mantle rocks: Influence of temperature, pressure, and the deformation fabric. *Journal of Geophysical Research: Solid Earth*, *108*(B8).
Hirth, G., & Kohlstedt, D. (2004). Rheology of the upper mantle and the mantle

wedge: A view from the experimentalists. *Inside the Subduction Factory*, *138*, 83–105.

Hoggard, M. J., Czarnota, K., Richards, F. D., Huston, D. L., Jaques, A. L., & Ghelichkhan, S. (2020). Global distribution of sediment-hosted metals controlled by craton edge stability. *Nature Geoscience*, *13*(7), 504–510.

Höink, T., Jellinek, A. M., & Lenardic, A. (2011). Viscous coupling at the lithosphere-asthenosphere boundary. *Geochemistry, Geophysics, Geosystems*, *12*(10).

Holm, P. M., Grandvuinet, T., Friis, J., Wilson, J. R., Barker, A. K., & Plesner, S. (2008). An 40Ar-39Ar study of the Cape Verde hot spot: Temporal evolution in a semistationary plate environment. *Journal of Geophysical Research: Solid Earth*, *113*(B8).

Iaffaldano, G., Davies, D. R., & DeMets, C. (2018). Indian ocean floor deformation induced by the Reunion plume rather than the Tibetan Plateau. *Nature Geoscience*, *11*(5), 362–366.

Iaffaldano, G., & Lambeck, K. (2014). Pacific plate-motion change at the time of the Hawaiian-Emperor bend constrains the viscosity of Earth's asthenosphere. *Geophysical Research Letters*, *41*(10), 3398–3406.

Jain, C., Rozel, A. B., Tackley, P. J., Sanan, P., & Gerya, T. V. (2019). Growing primordial continental crust self-consistently in global mantle convection models. *Gondwana Research*, *73*, 96–122.

Jaupart, C., & Mareschal, J. (2005). Production from heat flow data. *The Crust*, *3*, 65–84.

Jones, T., Davies, D. R., Campbell, I., Iaffaldano, G., Yaxley, G., Kramer, S., & Wilson, C. (2017). The concurrent emergence and causes of double volcanic hotspot tracks on the Pacific plate. *Nature*, *545*(7655), 472.

Kaislaniemi, L., & van Hunen, J. (2014). Dynamics of lithospheric thinning and mantle melting by edge-driven convection: Application to Moroccan Atlas mountains. *Geochemistry, Geophysics, Geosystems*, *15*(8), 3175–3189.

Katsura, T., Yoneda, A., Yamazaki, D., Yoshino, T., & Ito, E. (2010). Adiabatic temperature profile in the mantle. *Physics of the Earth and Planetary Interiors*, *183*(1-2), 212–218.

Katz, R. F., Spiegelman, M., & Langmuir, C. H. (2003). A new parameterization of hydrous mantle melting. *Geochemistry, Geophysics, Geosystems*, *4*(9).

Kennett, B., & Davies, D. (2020). Intra-plate volcanism in North Queensland and eastern new Guinea: A cryptic mantle plume? *Gondwana Research*, *79*, 209–216.

King, S. D., & Anderson, D. L. (1998). Edge-driven convection. *Earth and Planetary Science Letters*, *160*(3-4), 289–296.

King, S. D., & Ritsema, J. (2000). African hot spot volcanism: small-scale convection in the upper mantle beneath cratons. *Science*, *290*(5494), 1137–1140.

Klöcking, M., White, N., Maclennan, J., McKenzie, D., & Fitton, J. (2018). Quantitative relationships between basalt geochemistry, shear wave velocity, and asthenospheric temperature beneath western North America. *Geochemistry, Geophysics, Geosystems*, *19*(9), 3376–3404.

Korenaga, J., & Karato, S.-I. (2008). A new analysis of experimental data on olivine rheology. *Journal of Geophysical Research: Solid Earth*, *113*(B2).

Kramer, S. C., Wilson, C., Davies, R., Mathews, C., Gibson, A., Duvernay, T., … Ham, D. (2021). *Fluidityproject/fluidity: Zenodo release.* Zenodo. Retrieved from `https://doi.org/10.5281/zenodo.4896641` doi: 10.5281/zenodo.4896641

Kramer, S. C., Wilson, C. R., & Davies, D. R. (2012). An implicit free surface algorithm for geodynamical simulations. *Physics of the Earth and Planetary Interiors*, *194*, 25–37.

Lachenbruch, A. H. (1970). Crustal temperature and heat production: Implications of the linear heat-flow relation. *Journal of Geophysical Research*, *75*(17), 3291–3300.

Lau, H. C., Mitrovica, J. X., Austermann, J., Crawford, O., Al-Attar, D., & Latychev, K. (2016). Inferences of mantle viscosity based on ice age data sets: Radial structure. *Journal of Geophysical Research: Solid Earth*, *121*(10), 6991–7012.

Lenardic, A., & Moresi, L.-N. (1999). Some thoughts on the stability of cratonic lithosphere: Effects of buoyancy and viscosity. *Journal of Geophysical Research: Solid Earth*, *104*(B6), 12747–12758.

Le Voci, G., Davies, D. R., Goes, S., Kramer, S. C., & Wilson, C. R. (2014). A systematic 2-D investigation into the mantle wedge's transient flow regime and thermal structure: Complexities arising from a hydrated rheology and thermal buoyancy. *Geochemistry, Geophysics, Geosystems*, *15*(1), 28–51.

Liu, D., & Chen, L. (2019). Edge-driven convection and thinning of craton lithosphere: Two-dimensional thermal-mechanical modeling. *Science China Earth Sciences*, *62*(12), 2106–2120.

Mathews, C. (2021). *Methods for tracking material properties within an unstructured, adaptive mesh computational modelling framework, with application to simulating the development of seismic anisotropy at spreading centres and transform faults* (Unpublished doctoral dissertation). Australian National University.

McKenzie, D. (1984). The generation and compaction of partially molten rock. *Journal of Petrology*, *25*(3), 713–765.

McLaren, S., Sandiford, M., Hand, M., Neumann, N., Wyborn, L., & Bastrakova, I. (2003). The hot southern continent: heat flow and heat production in Australian Proterozoic terranes. *Special Papers-geological Society of America*, 157–168.

Missenard, Y., & Cadoux, A. (2012). Can Moroccan Atlas lithospheric thinning and volcanism be induced by edge-driven convection? *Terra Nova*, *24*(1), 27–33.

Mitrovica, J. X., & Forte, A. (2004). A new inference of mantle viscosity based upon joint inversion of convection and glacial isostatic adjustment data. *Earth and Planetary Science Letters*, *225*(1-2), 177–189.

Morgan, W. J. (1971). Convection plumes in the lower mantle. *Nature*, *230*(5288), 42.

Müller, R. D., Seton, M., Zahirovic, S., Williams, S. E., Matthews, K. J., Wright, N. M., ... others (2016). Ocean basin evolution and global-scale plate reorganization events since Pangea breakup. *Annual Review of Earth and Planetary Sciences*, *44*, 107–138.

Nicolaysen, L., Hart, R., & Gale, N. (1981). The Vredefort radioelement profile extended to supracrustal strata at Carletonville, with implications for continental heat flow. *Journal of Geophysical Research: Solid Earth*, *86*(B11), 10653–10661.

Parsons, B., & Sclater, J. G. (1977). An analysis of the variation of ocean floor bathymetry and heat flow with age. *Journal of geophysical research*, *82*(5), 803–827.

Paulson, A., & Richards, M. A. (2009). On the resolution of radial viscosity structure in modelling long-wavelength postglacial rebound data. *Geophysical Journal International*, *179*(3), 1516–1526.

Peacock, S. A. (1990). Fluid processes in subduction zones. *Science*, *248*(4953), 329–337.

Phipps Morgan, J., Morgan, W. J., Zhang, Y.-S., & Smith, W. H. (1995). Observational hints for a plume-fed, suboceanic asthenosphere and its role in mantle convection. *Journal of Geophysical Research: Solid Earth*, *100*(B7), 12753–12767.

Phipps Morgan, J., Parmentier, E., & Lin, J. (1987). Mechanisms for the origin of mid-ocean ridge axial topography: Implications for the thermal and mechanical structure of accreting plate boundaries. *Journal of Geophysical Research: Solid Earth*, *92*(B12), 12823–12836.

Pollack, H. N., & Chapman, D. S. (1977). On the regional variation of heat flow, geotherms, and lithospheric thickness. *Tectonophysics*, *38*(3-4), 279–296.

Priestley, K., McKenzie, D., & Ho, T. (2018). A lithosphere-asthenosphere boundary–a global model derived from multimode surface-wave tomography and petrology. *Lithospheric discontinuities*, 111–123.

Putirka, K. (2016). Rates and styles of planetary cooling on Earth, Moon, Mars, and Vesta, using new models for oxygen fugacity, ferric-ferrous ratios, olivine-liquid Fe-Mg exchange, and mantle potential temperature. *American Mineralogist*, *101*(4), 819–840.

Rawlinson, N., Davies, D. R., & Pilia, S. (2017). The mechanisms underpinning Cenozoic intraplate volcanism in eastern Australia: Insights from seismic tomography and geodynamic modeling. *Geophysical Research Letters*, *44*(19), 9681–9690.

Richards, M. A., Duncan, R. A., & Courtillot, V. E. (1989). Flood basalts and hotspot tracks: plume heads and tails. *Science*, *246*(4926), 103–107.

Richards, M. A., Yang, W.-S., Baumgardner, J. R., & Bunge, H.-P. (2001). Role of a low-viscosity zone in stabilizing plate tectonics: Implications for comparative terrestrial planetology. *Geochemistry, Geophysics, Geosystems*, *2*(8).

Roult, G., Peltier, A., Taisne, B., Staudacher, T., Ferrazzini, V., Di Muro, A., et al. (2012). A new comprehensive classification of the Piton de la Fournaise activity spanning the 1985–2010 period. search and analysis of short-term precursors from a broad-band seismological station. *Journal of Volcanology and Geothermal Research*, *241*, 78–104.

Rudolph, M. L., Lekić, V., & Lithgow-Bertelloni, C. (2015). Viscosity jump in Earth's mid-mantle. *Science*, *350*(6266), 1349–1352.

Sarafian, E., Gaetani, G. A., Hauri, E. H., & Sarafian, A. R. (2017). Experimental constraints on the damp peridotite solidus and oceanic mantle potential temperature. *Science*, *355*(6328), 942–945.

Schatz, J. F., & Simmons, G. (1972). Thermal conductivity of earth materials at high temperatures. *Journal of Geophysical Research*, *77*(35), 6966–6983.

Sengör, A., & Burke, K. (1978). Relative timing of rifting and volcanism on Earth and its tectonic implications. *Geophysical Research Letters*, *5*(6), 419–421.

Stotz, I. L., Iaffaldano, G., & Davies, D. R. (2017). Late Miocene Pacific plate kinematic change explained with coupled global models of mantle and lithosphere dynamics. *Geophysical Research Letters*, *44*, 7177-7186.

Stotz, I. L., Iaffaldano, G., & Davies, D. R. (2018). Pressure-driven Poiseuille flow: A major component of the torque-balance governing Pacific plate motion. *Geophysical Research Letters*, *45*(1), 117–125.

Tackley, P. J., Stevenson, D. J., Glatzmaier, G. A., & Schubert, G. (1993). Effects of an endothermic phase transition at 670 km depth in a spherical model of convection in the Earth's mantle. *Nature*, *361*(6414), 699.

Tatsumi, Y., Hamilton, D., & Nesbitt, R. (1986). Chemical characteristics of fluid phase released from a subducted lithosphere and origin of arc magmas: evidence from high-pressure experiments and natural rocks. *Journal of Volcanology and Geothermal Research*, *29*(1-4), 293–309.

Thordarson, T., & Höskuldsson, Á. (2008). Postglacial volcanism in Iceland. *Jökull*, *58*(198), e228.

Till, C. B., Elkins-Tanton, L. T., & Fischer, K. M. (2010). A mechanism for low-extent melts at the lithosphere-asthenosphere boundary. *Geochemistry, Geophysics, Geosystems*, *11*(10).

van den Hove, J. C., Van Otterloo, J., Betts, P. G., Ailleres, L., & Cas, R. A. (2017). Controls on volcanism at intraplate basaltic volcanic fields. *Earth*

and Planetary Science Letters, *459*, 36–47.
van Hunen, J., Huang, J., & Zhong, S. (2003). The effect of shearing on the onset and vigor of small-scale convection in a Newtonian rheology. *Geophysical research letters*, *30*(19).
Wilson, C. (2009). *Modelling multiple-material flows on adaptive unstructured meshes* (Unpublished doctoral dissertation). Imperial College London.
Ye, Y., Schwering, R. A., & Smyth, J. R. (2009). Effects of hydration on thermal expansion of forsterite, wadsleyite, and ringwoodite at ambient pressure. *American Mineralogist*, *94*(7), 899–904.

Supporting Information for 'Linking Intra-Plate Volcanism to Lithospheric Structure and Asthenospheric Flow'

DOI: 10.1002/2021GC009953

Thomas Duvernay[1], D. Rhodri Davies[1], Christopher R. Mathews[1], Angus H. Gibson[1], Stephan C. Kramer[2]

[1]Research School of Earth Sciences, The Australian National University, Canberra, ACT, Australia

[2]Department of Earth Science and Engineering, Imperial College London, London, UK

Contents of this file

Corresponding author: Thomas Duvernay, Research School of Earth Sciences, The Australian National University, 142 Mills Rd, Acton ACT 0200, Australia. (thomas.duvernay@anu.edu.au)

Melting Parameterisation

McKenzie (1984) defined a framework to calculate the amount of melt produced through decompression at constant entropy. Writing the total differential of entropy as a function of temperature, pressure and melt fraction, the following two governing equations are obtained:

$$\left.\frac{dF}{dP}\right|_S = \frac{-\frac{c_P}{T}\left.\frac{dT}{dP}\right|_F + \frac{\alpha_s}{\rho_s} + F\left(\frac{\alpha_f}{\rho_f} - \frac{\alpha_s}{\rho_s}\right)}{\Delta S + \frac{c_P}{T}\left.\frac{dT}{dF}\right|_P}, \tag{1}$$

$$\left.\frac{dT}{dP}\right|_S = \frac{\frac{\alpha_s}{\rho_s} + F\left(\frac{\alpha_f}{\rho_f} - \frac{\alpha_s}{\rho_s}\right) - \Delta S\left.\frac{dF}{dP}\right|_S}{\frac{c_P}{T}}. \tag{2}$$

In the above expressions, P, T and F represent the pressure, temperature and fraction of melt, respectively. The coefficient of thermal expansion, density and the specific heat at constant pressure are denoted by α, ρ and c_P, while S corresponds to entropy and ΔS to the entropy of fusion. Subscripts s and f differentiate between the solid and fluid phase, respectively, while derivative sub-scripts indicate variables that are held constant.

In the absence of melting, Equations 1 and 2 become:

$$\left.\frac{dF}{dP}\right|_S = 0, \tag{3}$$

$$\left.\frac{dT}{dP}\right|_S = \frac{\alpha_s T}{\rho_s c_P}. \tag{4}$$

In particular, Equation 4 represents the temperature change of a parcel of rock ascending adiabatically through Earth's mantle. However, in our numerical models, we can already calculate a temperature change as we are solving the heat equation for temperature. To ensure consistency between the evolution of temperature obtained through the melting framework and the thermal state of our model, we modify the framework's governing equations: we replace the adiabatic gradient term by the actual temperature gradient derived from the temperature field calculated by Fluidity. Mathematically, using thermodynamical identities, our modification translates to

$$\frac{\alpha}{\rho} = -\left.\frac{dS}{dP}\right|_T = \left.\frac{dS}{dT}\right|_P \left.\frac{dT}{dP}\right|_S \sim \frac{c_P}{T} \left.\frac{dT}{dP}\right|^{Fluidity},$$

and, in the absence of melting, it leads to

$$\left.\frac{dT}{dP}\right|_S \sim \left.\frac{dT}{dP}\right|^{Fluidity}.$$

Incorporating this change within Equations 1 and 2, we obtain the following system of coupled equations:

$$\left.\frac{dF}{dP}\right|_S = \frac{\left.\frac{dT}{dP}\right|^{Fluidity} - \left.\frac{dT}{dP}\right|_F^{Katz}}{\frac{T\Delta S}{c_P} + \left.\frac{dT}{dF}\right|_P^{Katz}} \tag{5}$$

$$\left.\frac{dT}{dP}\right|_S = \left.\frac{dT}{dP}\right|^{Fluidity} - \frac{T\Delta S}{c_P} \left.\frac{dF}{dP}\right|_S. \tag{6}$$

In the above expressions, derivative super-scripts signal where the expression/value for the derivative is sourced from.

References

McKenzie, D. (1984). The generation and compaction of partially molten rock. *Journal of Petrology*, *25*(3), 713–765.

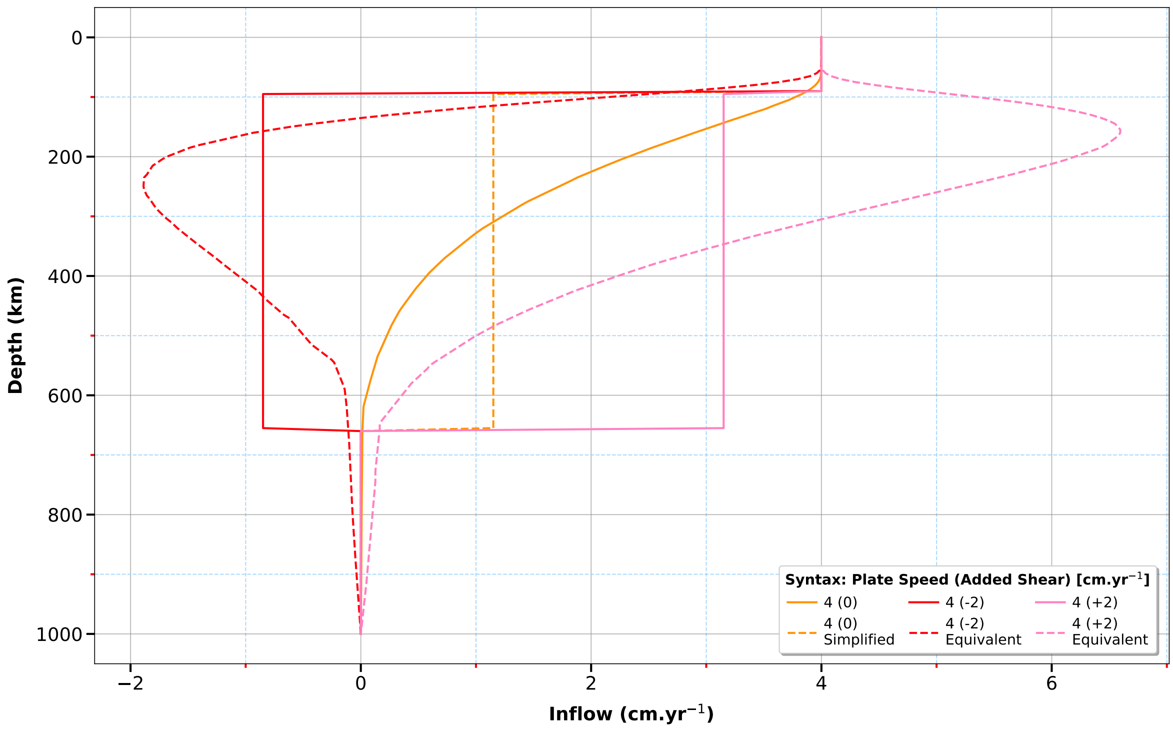

Figure S1. Velocity inflow profiles considered in the study (solid lines) and their counterparts used to demonstrate equivalent flow patterns (dashed lines). The '4 (0)' profile is measured within the oceanic realm of the purely plate-driven model. The '4 (0) Simplified' profile corresponds to a step-like version of the '4 (0)' profile, with plate velocity imposed from the surface down to 90 km (our initial LAB), constant velocity imposed within the asthenosphere (where the integral of velocity is identical to the '4 (0)' profile over this depth range), and zero flow imposed in the lower mantle. Profiles '4 (-2)' and '4 (+2)' build on the '4 (0) Simplified' profile by adding 2 cm yr^{-1} asthenospheric shear, either aligned with (+2) or opposite to (-2) plate motion. Profiles '4 (-2) Equivalent' and '4 (+2) Equivalent' are measured within the oceanic realm, from simulations where the '4 (-2)' and '4 (+2)' profiles are imposed at the inflow boundary.

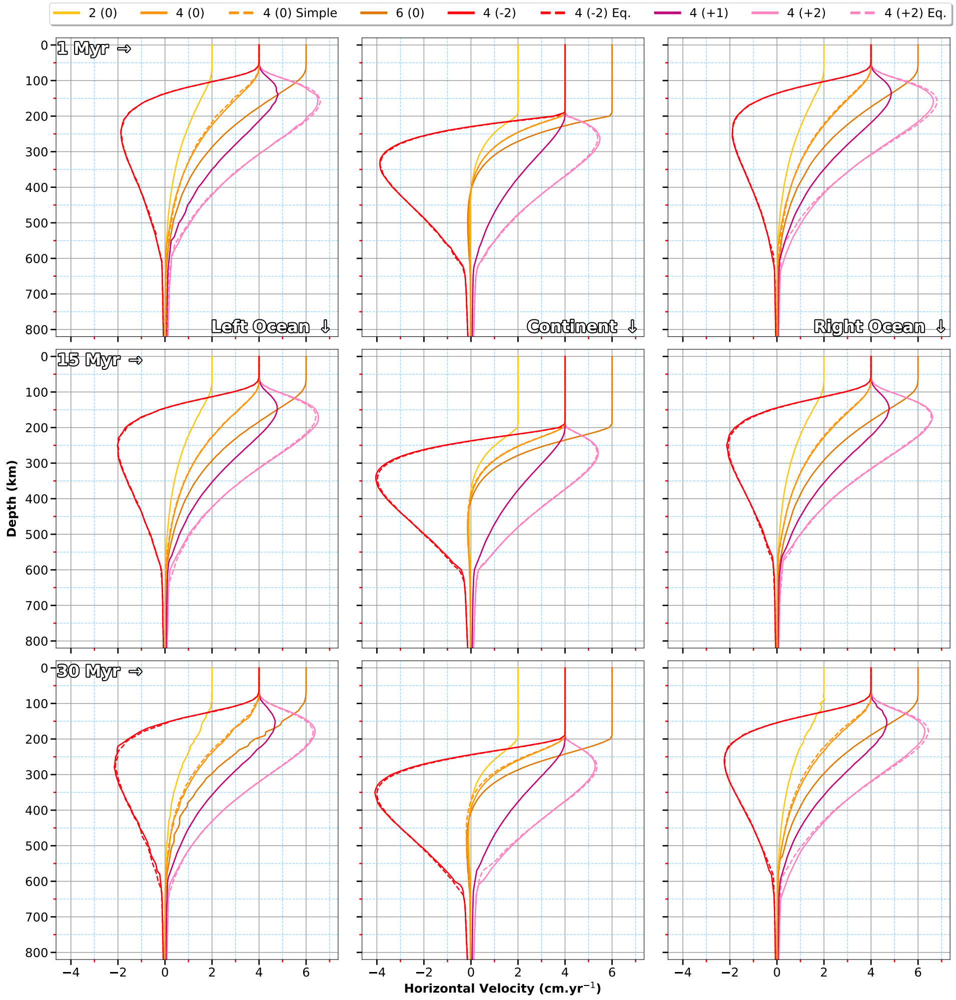

Figure S2. Velocity profiles generated within the numerical domain when plate motion and, in some cases, additional asthenospheric shear, are prescribed. Specifically, the profiles displayed in Figure S1 are prescribed as inflow boundary conditions for different models, in addition to cases with increased ('6 (0)') or decreased ('2 (0)') plate velocities. The resulting flow field is sampled below oceanic lithosphere to the left of the continent (left), below the continent (centre) and below oceanic lithosphere to the right of the continent (right). Additionally, different rows display profiles measured at 1 Myr, 15 Myr and 30 Myr, respectively. We find that cases where simplified step-function profiles are imposed at the inflow boundary yield results that are practically indistinguishable from the smoother profiles. This demonstrates that results are largely insensitive to the depth-dependence of the inflow profile prescribed within the asthenosphere – the flow is redistributed in line with the underlying physics.

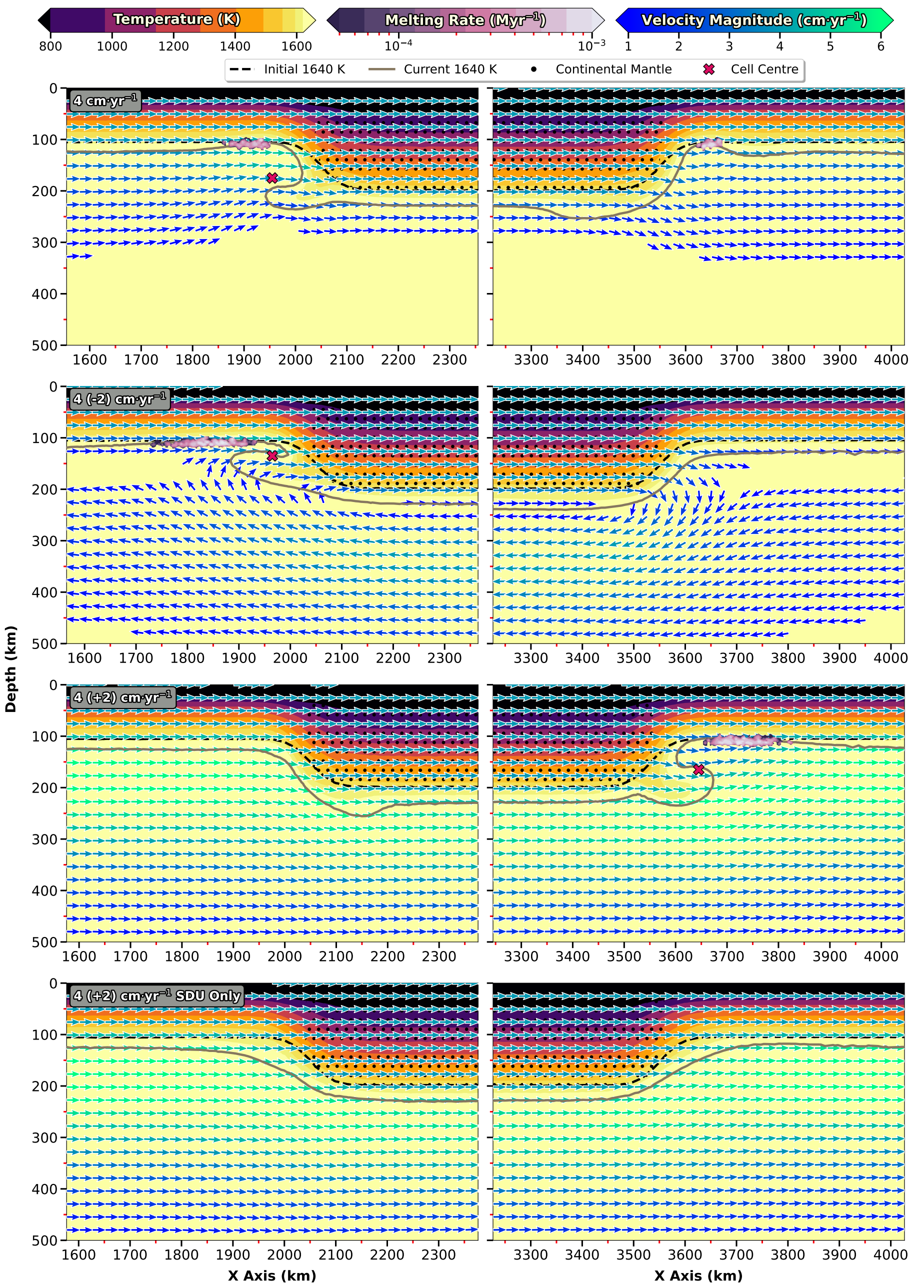

Figure S3. Effect of plate motion and asthenospheric flow on dynamics adjacent to lithospheric steps. The top row illustrates our $4\,\mathrm{cm\,yr^{-1}}$ purely plate-driven scenario, while the subsequent two rows display results following the addition of momentum within the asthenosphere, opposite to and aligned with plate motion, respectively. The bottom row is equivalent to the third row, except that the coefficient of thermal expansion has been set to 0; all models are displayed after 20 Myr. Graphic illustration similar to Figure 4, with glyphs only drawn where velocities exceed $1\,\mathrm{cm\,yr^{-1}}$; the velocity field is that directly output from the model.

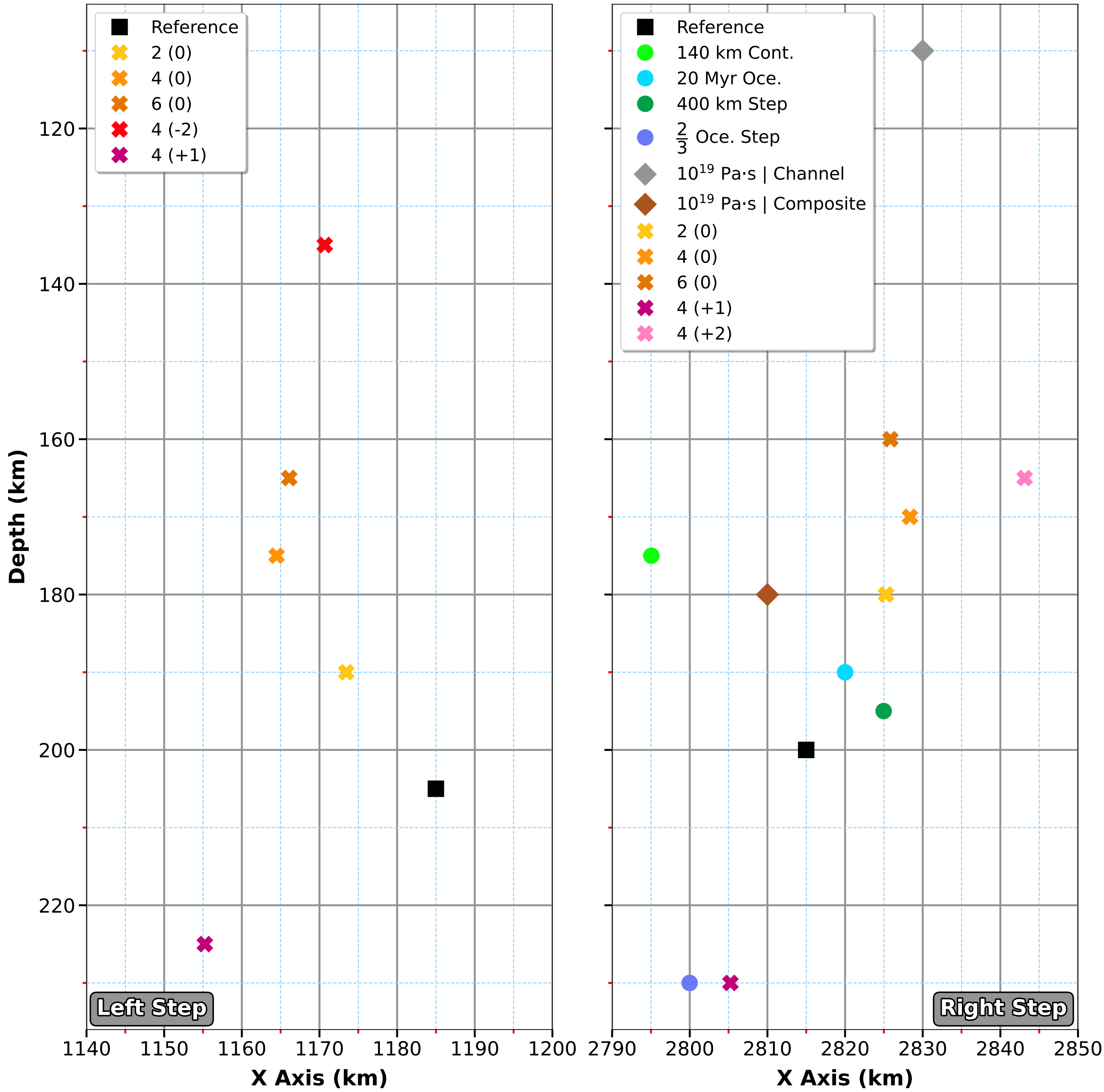

Figure S4. Location of cell centres used as a basis for vertical velocity profiles in Figure 5, determined at the time of maximum downwelling velocity as illustrated in Figure S5. Cases with plate motion are corrected for plate advection through time.

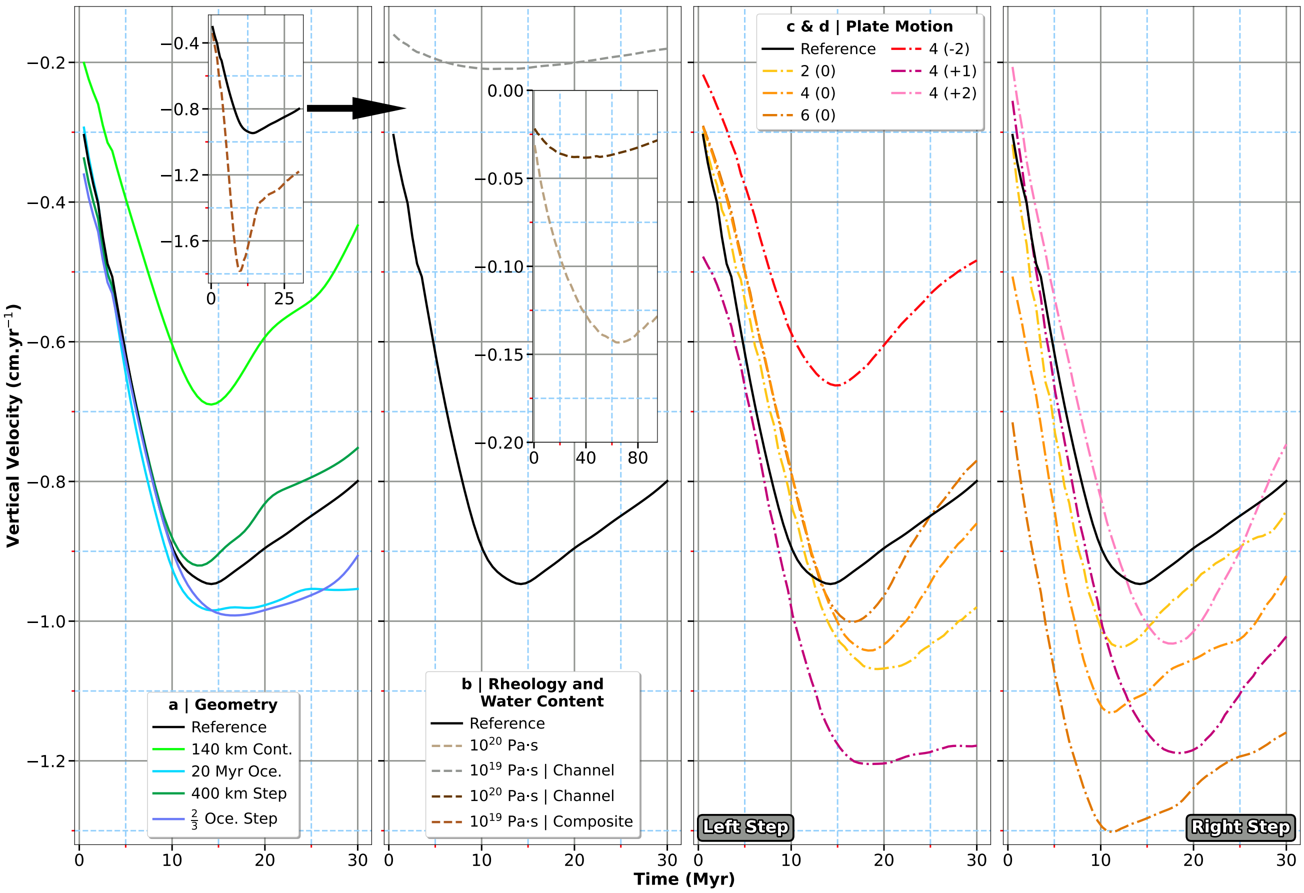

Figure S5. Maximum downwelling velocity, as a function of time, at the right step (if not specified). The velocity field is analysed over an area surrounding the step, no deeper than continental depth. Each curve has a local minimum, which we use to determine the time at which we compare the vigour of edge-driven instabilities cases across our chosen parameter space (Figure 5). Such a strategy allows for a meaningful comparison between different cases. (a) Effect of step geometry. The inset compares the reference case to the composite rheology model and, therefore, belongs with the cases shown on panel b as indicated by the black arrow. (b) Role of viscosity. The inset corresponds to a zoom on the 10^{20} Pa s cases, with a similar aspect ratio as the original panel. (c) & (d) Influence of plate motion and asthenospheric shear.

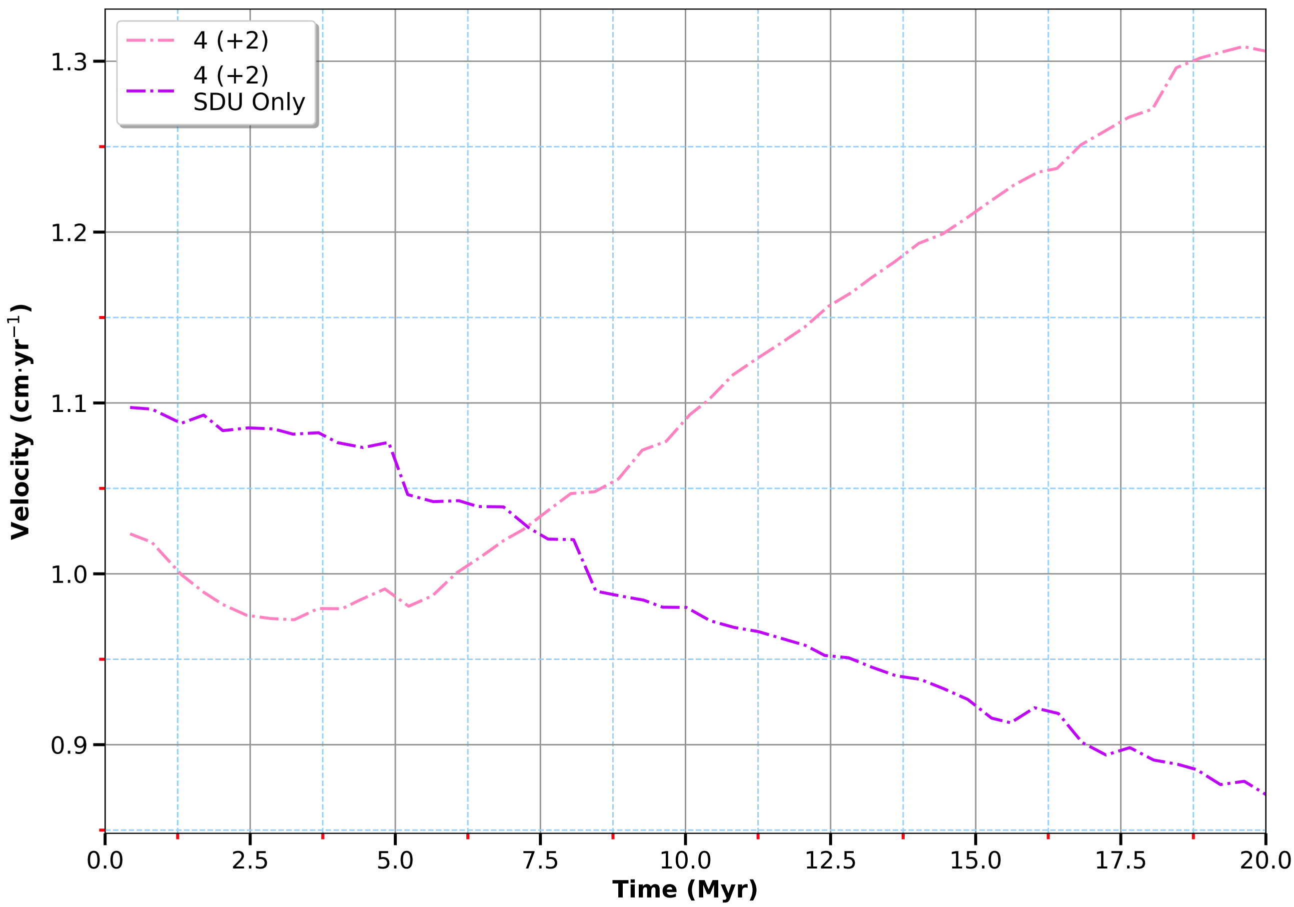

Figure S6. Temporal evolution of the maximum upwelling velocity recorded at the right step for cases with additional asthenospheric shear of $2\,\mathrm{cm\,yr^{-1}}$ prescribed at the inflow boundary. Case '4 (+2)' incorporates both EDC and SDU mechanisms, while case '4 (+2) SDU Only' solely features SDU (the coefficient of thermal expansion is set to 0).

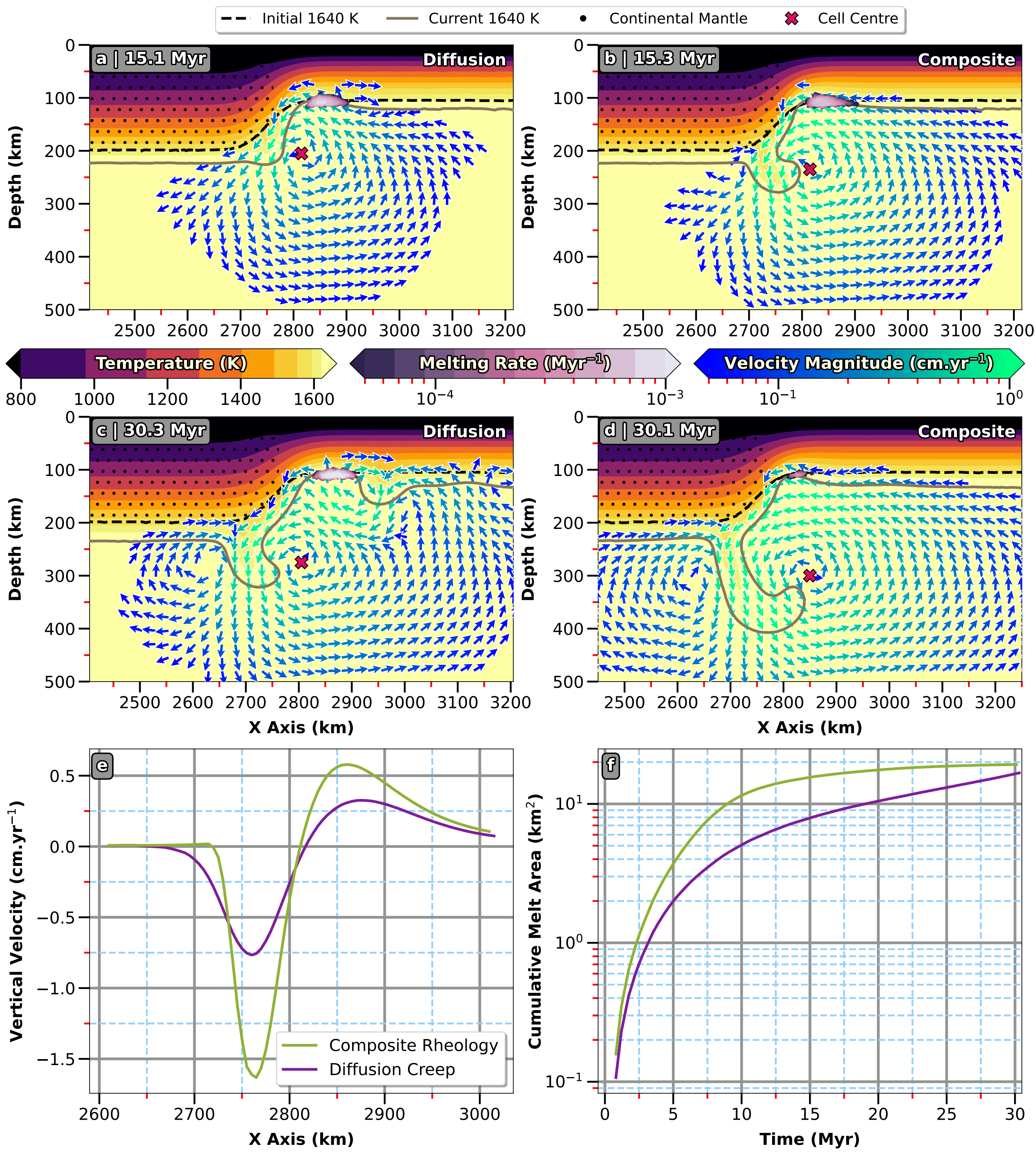

Figure S7. Dynamics (a-e) and melt production (f) compared between the reference case (a & c) and the model incorporating a composite rheology (b & d).

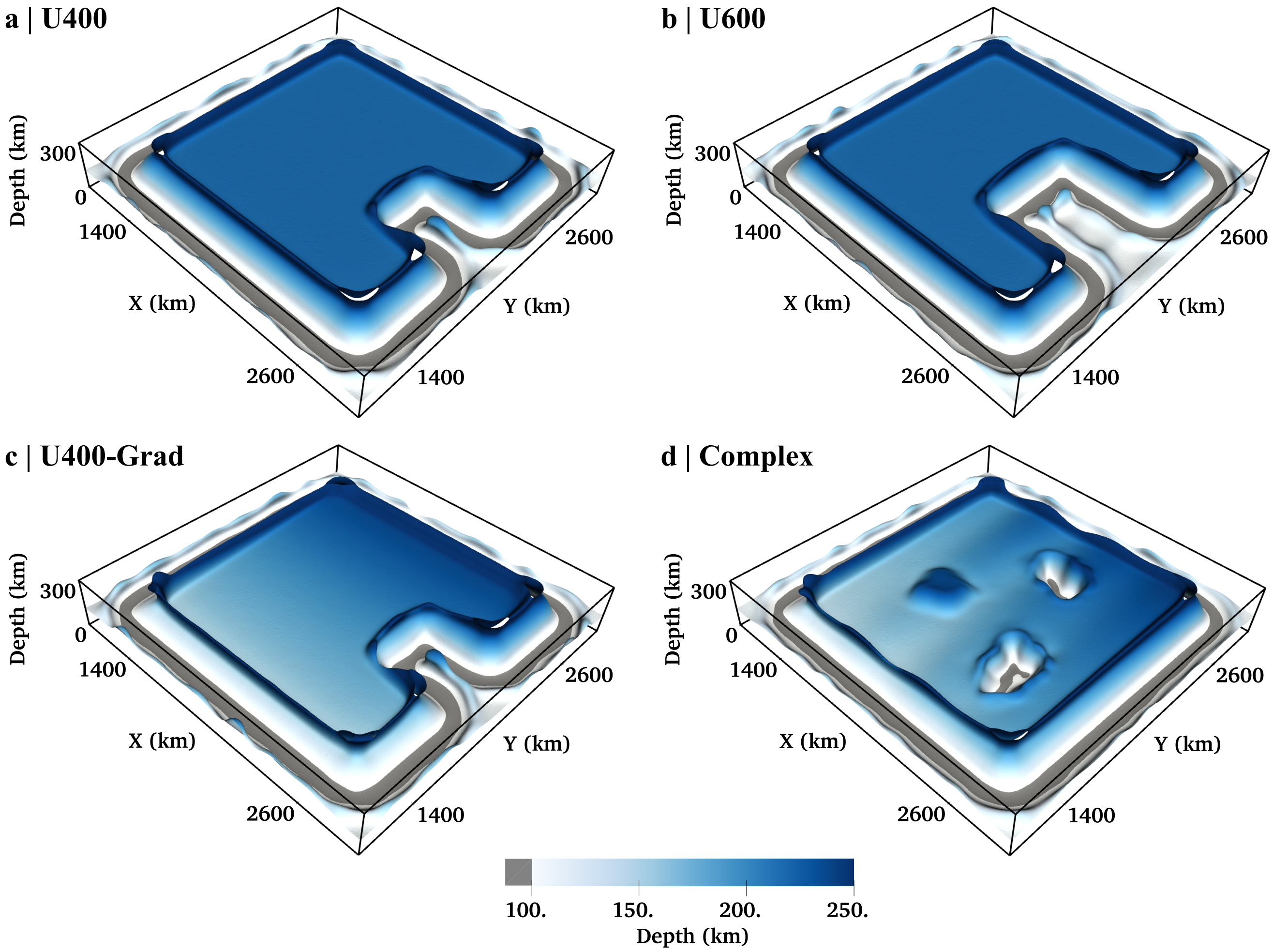

Figure S8. Topography at the LAB, as delineated by the 1620 K isotherm, for continental geometries used in 3-D simulations. Cases are illustrated after 30 Myr of model evolution. (a) Case U400. (b) Case U600. (c) Case U400-Grad. (d) Case Complex.

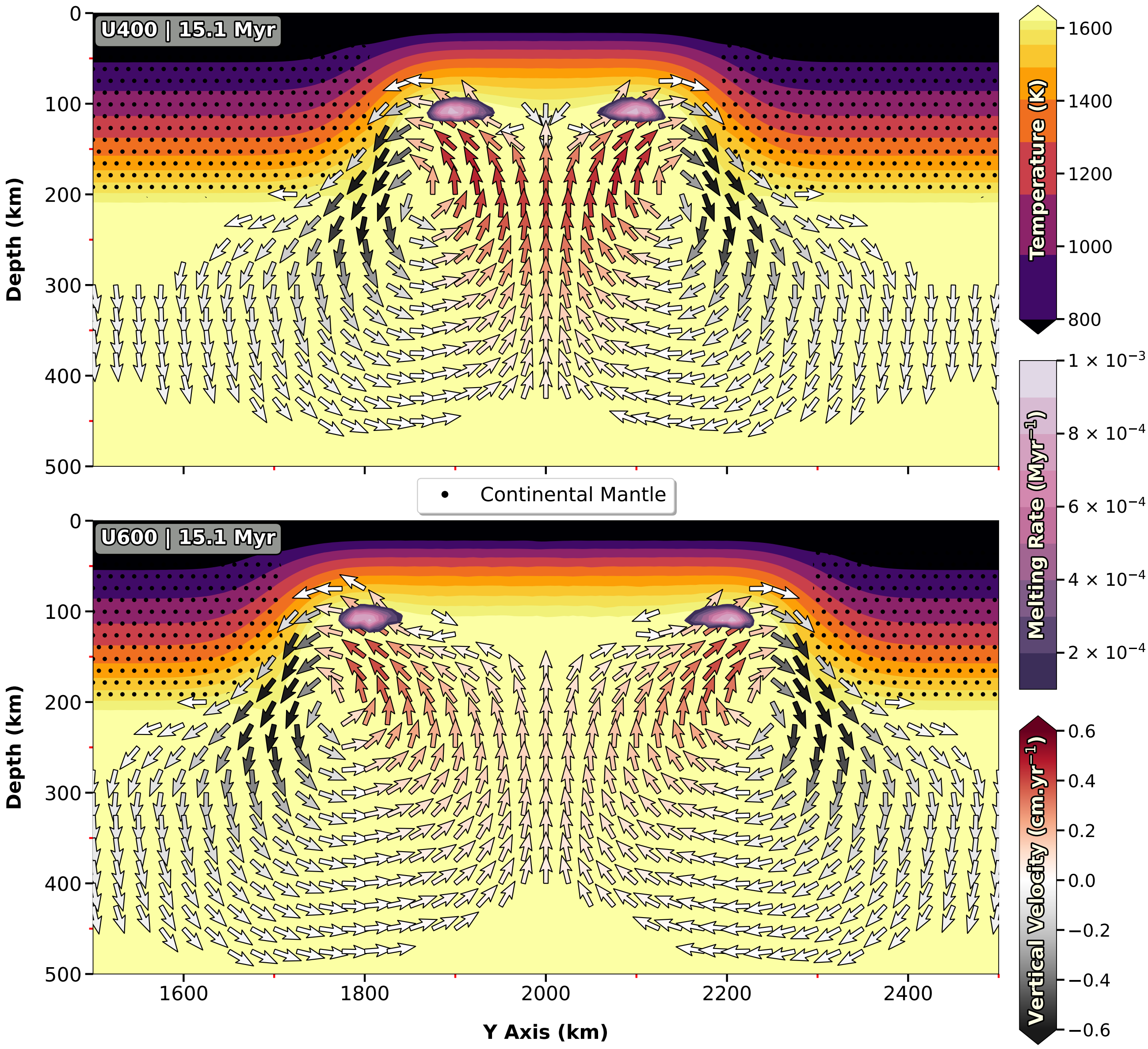

Figure S9. Influence of the indent's width on the flow dynamics, as observed after 15 Myr. Background colours represent temperature. Black dots depict the location of continental mantle. Arrow glyphs illustrate the velocity field and their colour indicates the strength of flow. Areas experiencing melting are represented as a superimposed surface, coloured by melting rate.

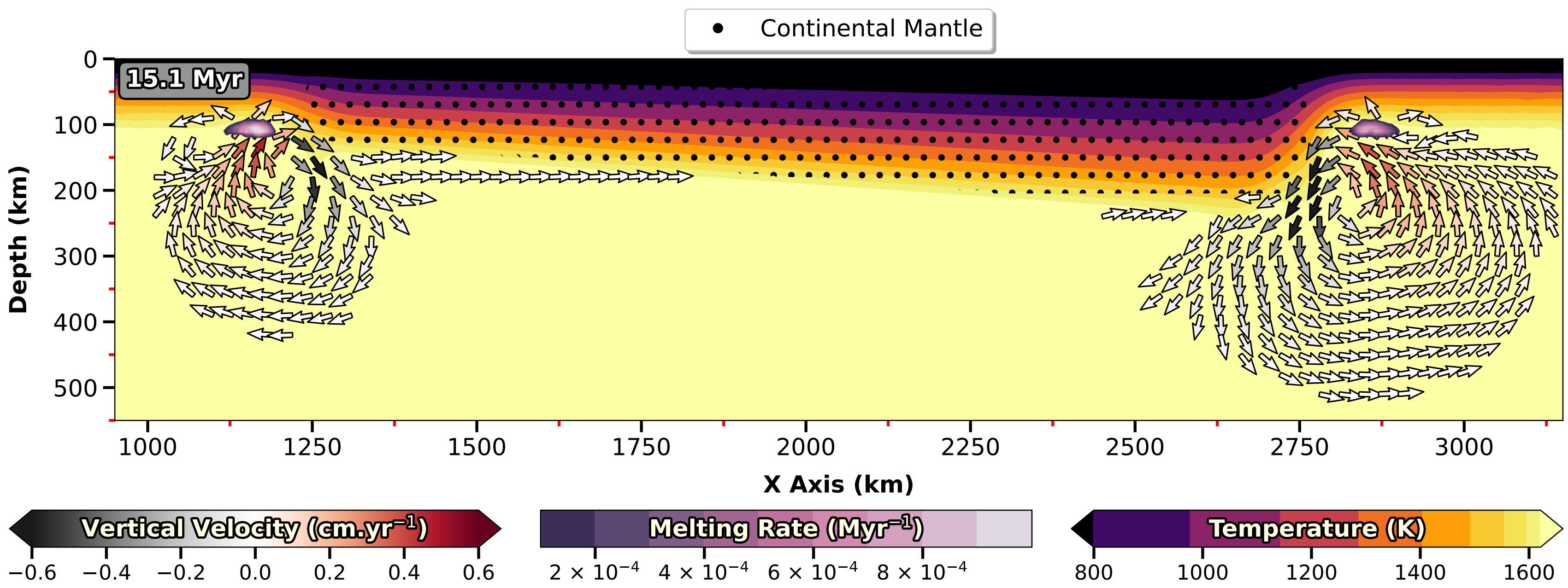

Figure S10. Effect of continental thickness on edge-driven cell development, as observed after 15 Myr for Case U400-Grad. Background colours represent temperature. Black dots depict the location of continental mantle. Arrow glyphs illustrate the velocity field and their colour indicates the strength of the flow. Particles that record active melting are represented by a superimposed surface, coloured by melting rate.

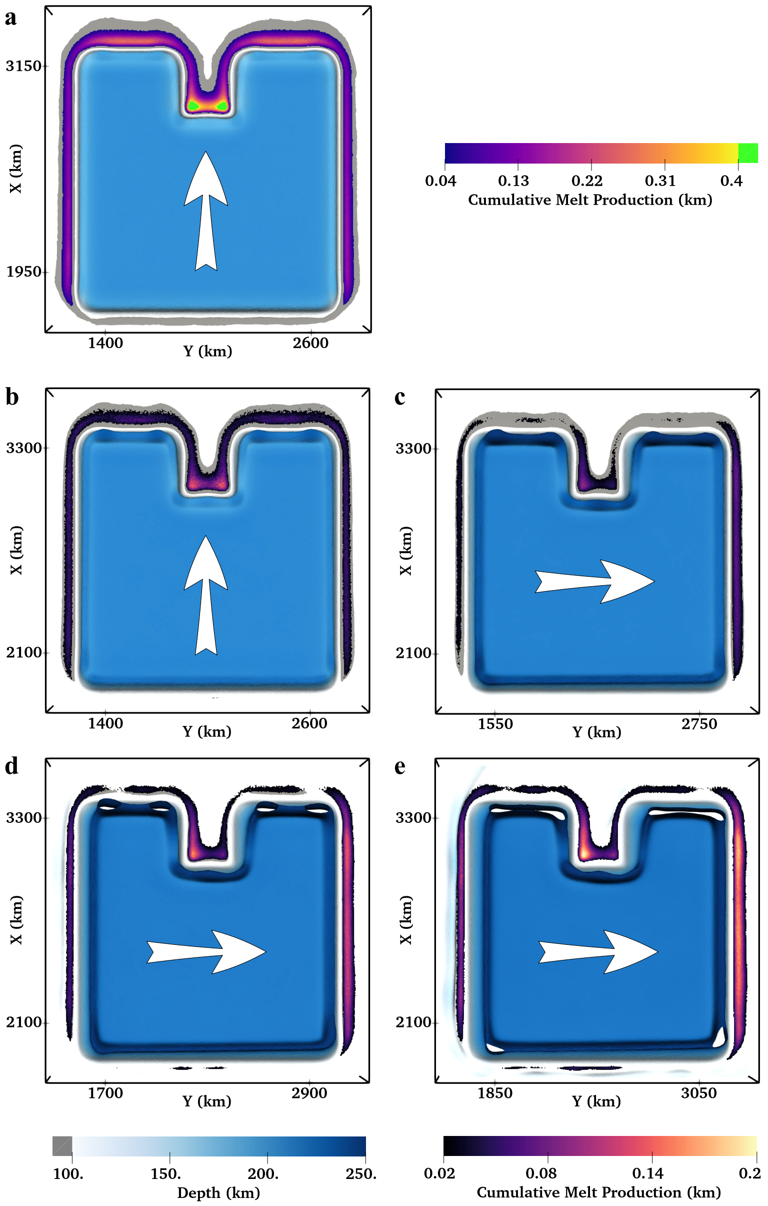

Figure S11. Melt production around the continent following a 90° change in prescribed plate motion and inflow direction at 16 Myr for the positive-x model. Large white arrows represent both the direction of plate motion and the direction of asthenospheric flow relative to the continent, and point from the continent's leading edge to its trailing edge. (a) Cumulative melt production after 12 Myr. (b) Cumulative melt production between 12 Myr and 16 Myr. (c) Cumulative melt production between 16 Myr and 20 Myr (i.e. immediately following the change in imposed flow direction). (d) Cumulative melt production between 16 Myr and 24 Myr. (e) Cumulative melt production between 16 Myr and 28 Myr.

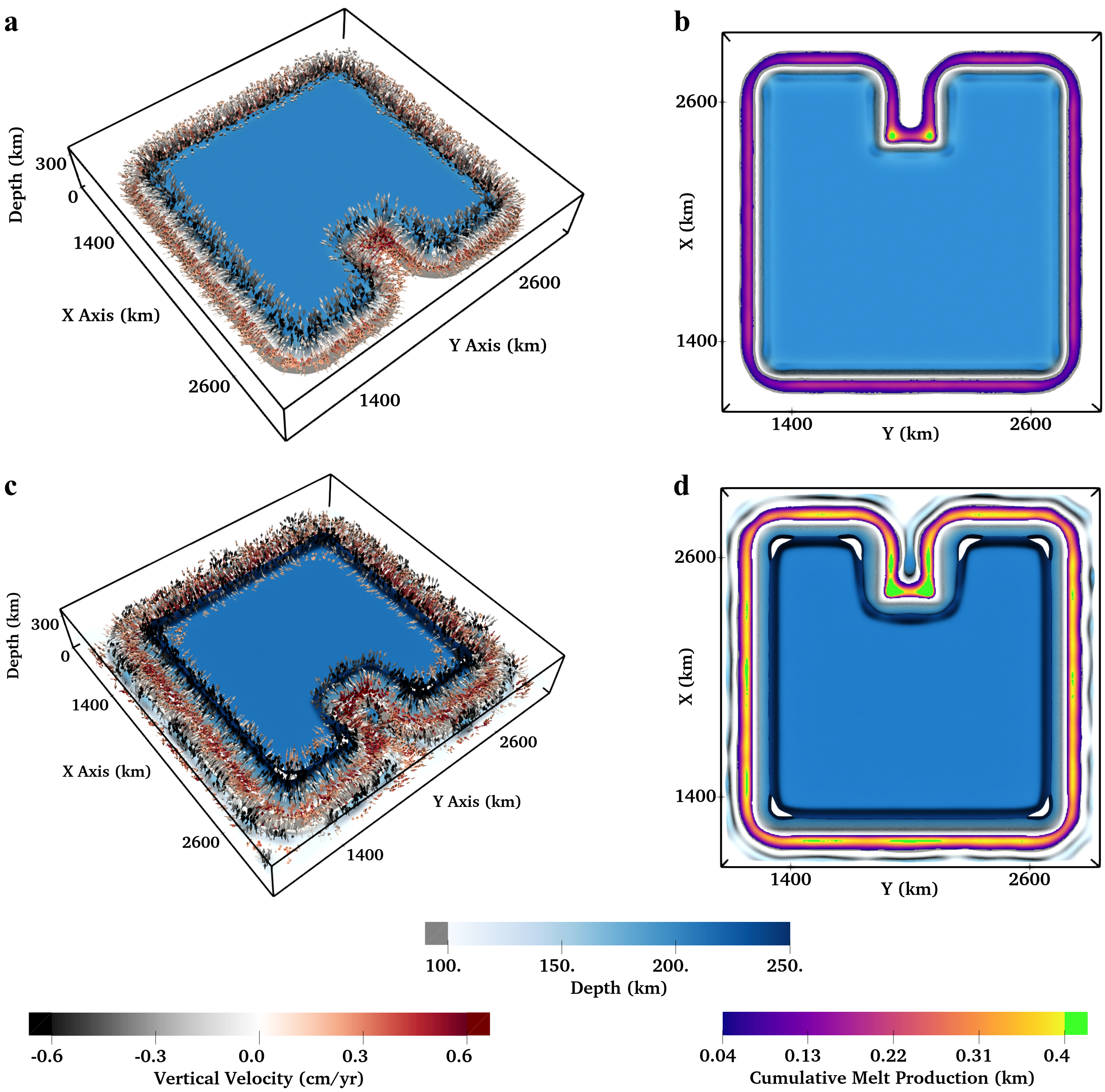

Figure S12. Comparison of the flow dynamics and melt production adjacent to the continent over time for Case U400. Graphic illustration is similar to Figures 7 and 8. (a) Velocity field after 15 Myr. (b) Cumulative melt production after 15 Myr. (c) Velocity field after 30 Myr. (d) Cumulative melt production after 30 Myr.